The Effect of a Dissipative Reservoir on the Dynamics of Delta-Kicked Oscillators

CCD Dissertation
FHS Mathematics and Computer Science Part C
Candidate no. 735325

Hilary Term 2016

Acknowledgements

I would like to thank Mason Porter for the help and guidance he provided me with over the course of this project.

Abstract

We study the field of quantum chaos, which involves quantum systems that exhibit chaotic behaviour in the classical limit. To approach this topic, we examine the quantisation of the delta-kicked oscillator, a well-known system with a Hamiltonian that consists of the harmonic oscillator coupled to a delta function that is periodic in time. We consider the system both in its commonly studied form and also with a different potential term related to the sawtooth function, and we compare our results for these two cases.

First we analyse the classical dynamics, using intuition from KAM theory to give a qualitative description of the result of increasing the coupling between the harmonic oscillator and the kick term. We quantise the system and determine approximate analytic expressions for the breaking time (the time of departure from the predictions of Ehrenfest's theorem) for both a weak and strong coupling strength. We give numerical evidence to support these expressions.

We present a well-known argument relating the kicked oscillator to the problem of an electron in a lattice and show how the phenomenon of Anderson localisation arises in the system, and give numerical evidence for this in the form of IPR calculations.

We study the kicked oscillator in the presence of a dissipative environment and show that (1) a sufficiently strong coupling to this environment can make the breaking time arbitrarily large and reduce the effect of localization, and (2) that complete quantum-classical correspondence is not possible in the chaotic regime.

The main result is a derivation for the breaking time in the case of the sawtooth potential, both in the system without an external environment (closed system) and when it is subject to dissipation (open system). We also present numerical calculations of the inverse participation ratio for both potentials.

Contents

1 Introduction

1.1 Classical and Quantum Chaos

Quantum chaos is a field of mathematics and physics concerned with quantum systems that exhibit chaotic behaviour in the classical limit.

There are numerous ways of defining chaos in the classical sense. The definition we will use in this dissertation concerns the maximum *Lyapunov exponent* (LE) of the system. For discrete dynamical systems with evolution equation $x_{n+1} = f(x_n)$ in an N-dimensional phase space there are N LEs characterising the rate of separation of nearby points along each axis of the system's phase space. The maximum of these is given by the equation

$$\lambda = \lim_{n\to\infty} \frac{1}{n} \sum_{i=0}^{\infty} \ln|f'(x_i)|. \tag{1.1}$$

We then call a system *chaotic* if this maximum exponent is positive and at least one of the other LEs is negative. This captures the idea of sensitive dependance on initial conditions that is usually part of an informal definition of chaos. However, there are other definitions of chaos, e.g. in terms of topological mixing properties [17].

We can also use the LEs to define a notion of dimension for the set on which the dynamical system lives. The *Kaplan–York dimension* (KY-dimension) of a dynamical system in $\mathbb{R}^N$ with LEs $\lambda_1 \geq \lambda_2 \geq \ldots \geq \lambda_N$ is [21]

$$D_{\mathrm{KY}} = j + \frac{\lambda_1 + \cdots + \lambda_j}{|\lambda_{j+1}|}, \tag{1.2}$$

where j is the largest integer for which $\lambda_1 + \cdots + \lambda_j \geq 0$. A non-integer KY-dimension suggests that this set is a *fractal* [26], a geometric shape that is self-similar on all scales.

We call a Hamiltonian system *integrable* if the Hamiltonian can be expressed only in terms of the action variable in *action–angle coordinates* [40]. Otherwise we call the system *non-integrable*. Chaos does not occur in integrable systems, though being non-integrable is not enough to ensure chaotic behaviour. We will explore this more in Chapter 3.

Due to the linearity (and integrability) of the Schrödinger equation, chaos does not occur in quantum systems in the same way that it does in classical systems. In fact, it may be more precise to say that quantum chaos is simply the study of non-integrable quantum systems.

1.2 The Delta-Kicked Oscillator

A commonly-studied model is the delta-kicked oscillator, which is well documented due to its relative simplicity, the fact that it exhibits many of the interesting phenomena associated with quantum chaos, and the ability to realise it experimentally [7, 24]. Classically, the kicked oscillator has Hamiltonian

$$H = \frac{p^2}{2m} + \frac{m\omega^2 x^2}{2} + AV(x) \sum_{n=-\infty}^{\infty} \delta(t - n\tau), \tag{1.3}$$

where τ is the period of the kicking potential, A is the kick strength, and $V(x)$ is a periodic (or quasi-periodic) potential. Most often, scholars consider the potential $V(x) = \cos(kx)$, but other

potentials can give rise to different dynamics that are less well studied, especially in the quantum regime [32]. In this dissertation, I will look at two different potentials. The first is the *cosine potential*

$$V(x) = \cos(kx). \tag{1.4}$$

Motivated by [44], we will also consider the potential given by the Fourier series

$$V(x) = \frac{\kappa x}{2} + \frac{\kappa^2}{2\pi^2} \sum_{j=1}^{\infty} \frac{1}{j^2} \cos\left(\frac{2j\pi x}{\kappa}\right), \tag{1.5}$$

which we will call the *sawtooth potential*. This potential lacks the symmetry of the cosine potential. In the classical case we will see that it is the derivative of the potential that matters, and the derivative of (1.5) is a sawtooth function of period κ:

$$\begin{aligned} V'(x) &= \frac{\kappa}{2} - \frac{\kappa}{\pi} \sum_{j=1}^{\infty} \frac{1}{j} \sin\left(\frac{2j\pi x}{\kappa}\right) \\ &= x - \kappa \left\lfloor \frac{x}{\kappa} \right\rfloor. \end{aligned} \tag{1.6}$$

Classically, the kicked oscillator with the potential (1.5) has been studied by Lowenstein [43, 44], but it has not been examined in the quantum regime to our knowledge.

Although the kicked oscillator (especially with the cosine potential) has been extensively discussed in the literature, the system in the presence of an external environment has been less well studied. As well as studying the system in isolation, we will also consider a dissipative environment modelled by a zero-temperature reservoir and discuss what effect this has on the dynamics in both the classical and quantum regimes. A system subject to such outside effects is called *open*, otherwise it is called *closed*.

We discuss our main course of study in the next sections.

1.3 Breaking Time

Loosely, Ehrenfest's Theorem states that quantum-mechanical expectation values obey Newton's classical equations of motion. Formally, given a quantum system with Hamiltonian $\hat{H}$ and an observable $\hat{A}$, the theorem states

$$\frac{d}{dt}\langle \hat{A} \rangle = \frac{1}{i\hbar}\langle [\hat{A}, \hat{H}] \rangle + \left\langle \frac{\partial \hat{A}}{\partial t} \right\rangle, \tag{1.7}$$

which reduces to Newton's equations when applied to the position and momentum operators.

It should come as no surprise that (1.7) is true only with some important caveats, such as the assumption that the system is classically integrable [54]. Schrödinger proved that this is indeed true for the standard harmonic oscillator [49], but in more general situations the correspondence may break down in time.

We call the time at which the correspondence first breaks down the *Ehrenfest time* or *breaking time* $t_\hbar$. For $t < t_\hbar$ a quantum wave packet follows the dynamics of a classical trajectory (guaranteed by Ehrenfest's theorem), but when $t > t_\hbar$ even a coherent wave packet may spread over

all of phase space or otherwise diverge from the predictions of classical physics. It is known that for kicked systems such as (1.3) in the chaotic regime and with maximum LE λ, the breaking time satisfies

$$t_\hbar \propto \lambda^{-1} \ln(\Delta^2 p/\hbar), \tag{1.8}$$

where $\Delta^2 p$ is the initial uncertainty in momentum [6].

The situation for the kicked oscillator when it is not in a chaotic regime is less clear, but there is evidence to suggest that $t_\hbar$ is of order $\hbar^{-1}$.

1.4 Localization

We say a quantum state is *localized* in a region Ω if the wavefunction decays exponentially outside of Ω. Localization can occur in position, momentum, or both, depending on the expression for the wavefunction in position/momentum space. By viewing the state as a probability distribution over basis states, one can think of a localized state as one in which most of the weight of the distribution is on a small number of basis states.

Localization can occur through various mechanisms. Quantum interference suppresses the classical diffusion of particles in some disordered systems, a phenomenon called *Anderson localization*. The phenomenon was first studied by Anderson, who suggested the possibility of electron localization inside a semiconductor and introduced a tight-binding model for the evolution of the wave function on a lattice. It has been shown that this kind of localization only requires a very low degree of disorder or randomness [27].

1.5 Outline

The remainder of this dissertation is organised as follows.

In Chapter 2, we overview the classical dynamics of the kicked oscillator, both for the closed system and in the presence of a dissipative environment. We use a KAM theory approach to analyse the transition from non-chaotic to chaotic behaviour.

In Chapter 3, we discuss the quantum dynamics of the closed system with a view towards gaining a deeper understanding of the classical dynamics and how they might arise from the quantum regime. Our main result is an expression for the breaking time of the system, but we will also consider localization and show that the system can be put in the form of a tight-binding model.

In Chapter 4, we study the quantum system in the presence of a dissipative reservoir. The main result of this section is an expression for the breaking time and the determination of parameter regions for which this is infinite. It is known that the presence of an environment can also suppress or enhance localization, and we will also investigate this issue.

In Chapter 5, we summarise the results obtained and offer some final remarks on quantum–classical correspondence in the presence of a dissipative environment. We also offer some suggestions for future work.

We present the code used for numerical simulations in the appendix.

2 Classical Dynamics

We begin by deriving the equations of motion for the kicked oscillator. With the Hamiltonian as in (1.3), Hamilton's equations of motion are

$$\frac{dx}{dt} = \frac{p}{m}, \qquad \frac{dp}{dt} = -m\omega^2 x - A\frac{dV}{dx}\sum_{n=-\infty}^{\infty}\delta(t - n\tau).$$

In between the kicks, the time evolution is exactly the same as for the standard harmonic oscillator. To deal with the kicks, we integrate the equation for dp/dt over some neighbourhood about the kick at $n\tau$ to derive the mapping

$$p((n+1)\tau) = p(n\tau) - AV'(x(n\tau)). \tag{2.1}$$

Combining Eq. (2.1) with the standard solution for the harmonic oscillator

$$\begin{aligned} x(t) &= x(0)\cos(\omega t) + \frac{p(0)}{m\omega}\sin(\omega t), \\ p(t) &= p(0)\cos(\omega t) + m\omega x(0)\sin(\omega t), \end{aligned}$$

and introducing the notation $x_n = x(n\tau)$, $p_n = p(n\tau)$, we obtain a mapping from the instant before the nth kick to the instsnt before the $(n+1)$st:

$$\begin{aligned} x_{n+1} &= x_n\cos(\omega\tau) + \frac{\sin(\omega\tau)}{m\omega}[p_n - AV'(x_n)], \\ p_{n+1} &= [p_n - AV'(x_n)]\cos(\omega\tau) - x_n m\omega\sin(\omega\tau). \end{aligned} \tag{2.2}$$

2.1 The Closed System

2.1.1 Cosine Potential

First we consider the cosine potential given by Eq. (1.4). By changing coordinates to a dimensionless position v and momentum u defined by

$$\begin{aligned} v &= kx, \\ u &= \frac{kp}{m\omega}, \end{aligned} \tag{2.3}$$

we obtain the nondimensionalised form of Eq. (2.2):

$$\begin{aligned} v_{n+1} &= v_n\cos(\alpha) + \sin(\alpha)[u_n + K\sin(v_n)] \\ u_{n+1} &= [u_n + K\sin(v_n)]\cos(\alpha) - v_n\sin(\alpha), \end{aligned} \tag{2.4}$$

where $K = Ak^2/(m\omega)$ is the renormalised kicking strength and $\alpha = \omega\tau$ is the ratio between the period of the kicks and the period of the oscillator. These are the only free parameters.

We take $\alpha = 2\pi/q$. When the *resonance condition* $q \in \mathbb{Q}$ is satisfied, there is rotational symmetry of order q, as we can see in Fig. (2.1a). When $q \in \{3, 4, 6\}$ there is crystal symmetry

given by a tessellation of the plane with triangles, squares, and hexagons respectively. This can be seen clearly in Fig. 2.1. Otherwise, there is quasicrystal symmetry, except in the degenerate cases $q = 1, 2$ [13].

The symmetric structure that arises is often called a *stochastic web* [58], as it takes the form of an interconnected web of unstable dynamics spread throughout phase space. Inside this web the motion is chaotic. As the parameter K increases the chaotic regions begin closer to the fixed points of (2.4) and cycles of the system (which fall in the centres of the 'cells'). Visually, the cells gradually become overtaken with regions of chaos [13]. Although some symmetry is lost, the q-fold rotational symmetry remains.

The choice of irrational q removes all traces of crystalline structure from the phase plane, producing a region of complete disorder (seen in Fig. 2.1b). For both rational and irrational q, the trajectories are unbounded in phase space.

We can also approximate the largest LE for the system using the standard approach given in [51]. As we stated in Chapter 1, a positive maximum LE is an indicator of chaos. Figure 2.2 shows that for some value of K, the maximal LE becomes postive and continues to grow as K becomes larger. We investigate the regions in which the maximal LE is 0 in more detail in Chapter 2.2.

Another helpful way of visualising the evolution of Eq. (2.4) is to examine the evolution of a probability distribution. This gives something that is easier to compare with the associated quantum system, where we cannot follow a single trajectory. The plots in Fig. 2.3 show the evolution of an initial set of points drawn from the Gaussian distribution, for various kick strengths. The centre part of the stochastic web in Fig. 2.1 is clearly visible in Fig. 2.3a.

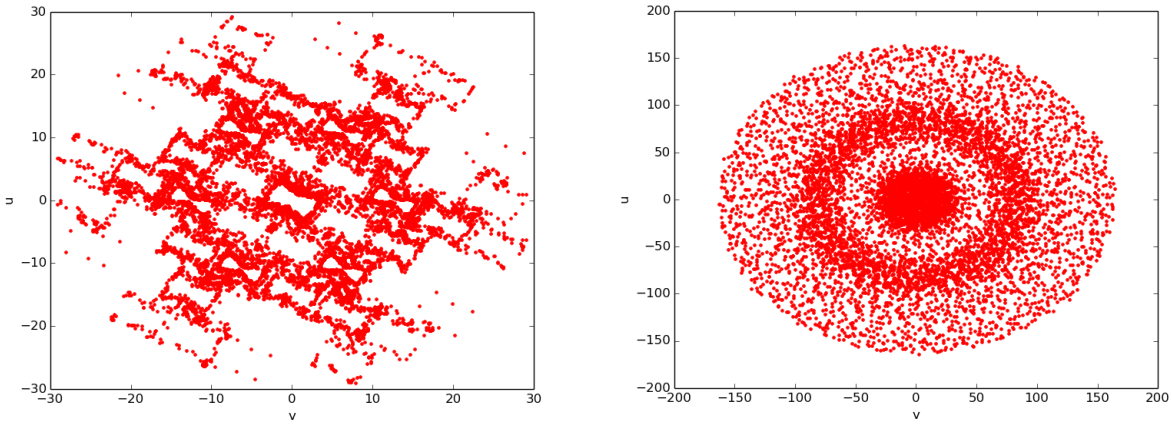

(a) $q = 6$.

(b) $q = \sqrt{2}$.

Figure 2.1: Plots of the mapping (2.4) for $K = 2$ and both a rational and irrational choice of q after 10000 kicks. For rational q, we observe a stochastic web structure that spreads unboundedly in phase space as $n \to \infty$. For irrational q, the phase space lacks the rotational symmetry, but the orbit still eventually fills the entire phase space.

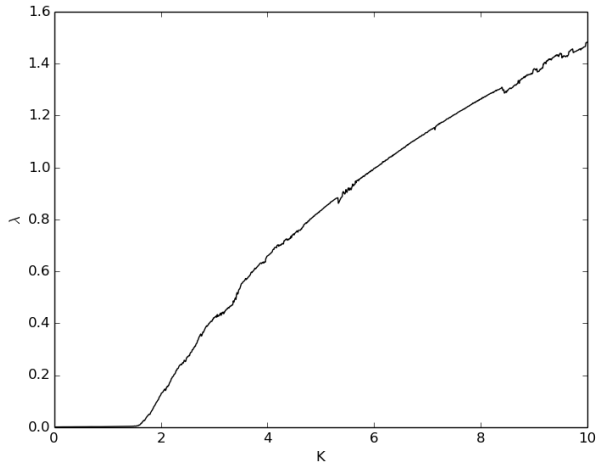

Figure 2.2: Maximal LE λ for the mapping (2.4) as a function of K for $q = 6$. It becomes positive at $K \approx 1.7$. A positive LE is an indicator of chaos.

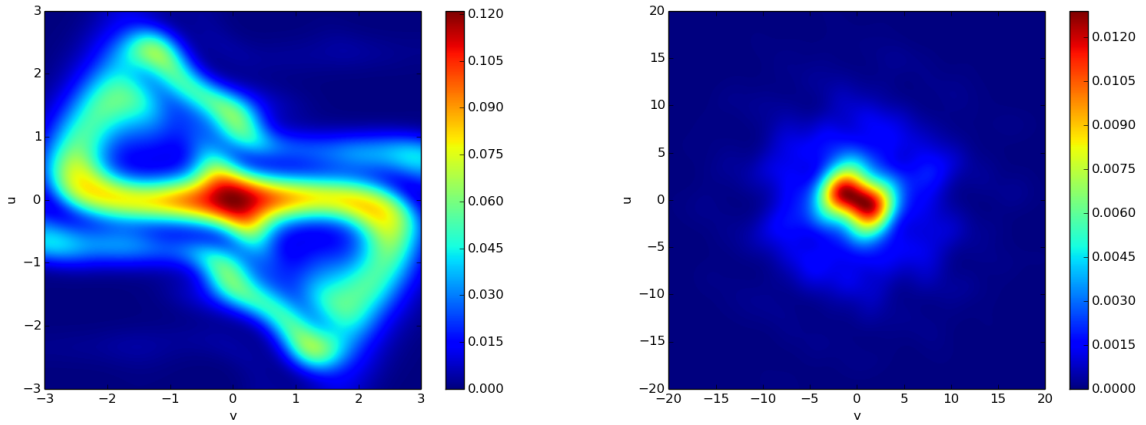

(a) $n = 9$. (b) $n = 500$.

Figure 2.3: Classical probability density function (PDF) for (a) $n = 9$ and (b) $n = 500$, with $K = 2$ and $q = 6$. The right image shows the stochastic web begining to emerge. We generated these plots by drawing an ensemble of 10^5 initial conditions from a Gaussian distribution with mean 0 and deviation 1, and then evolving them for n time steps using the mapping (2.4). We calculated the PDF for the evolved data was then calculated using kernel density estimation [50] and plotted on a 1000×1000 mesh grid.

2.1.2 Sawtooth Potential

We now analyse the sawtooth potential given by Eq. (1.5). Substituting this into Eq. (2.2) and changing to dimensionless quantities defined by

$$v = \frac{x}{\kappa},$$
$$u = \frac{p}{m\omega\kappa},$$

yields the mapping

$$\begin{aligned} v_{n+1} &= v_n \cos(\alpha) + \sin(\alpha)[u_n + L(\lfloor v_n \rfloor - v_n)], \\ u_{n+1} &= [u_n + L(\lfloor v_n \rfloor - v_n)] \cos(\alpha) - v_n \sin(\alpha), \end{aligned} \tag{2.5}$$

where $L = A/(m\omega)$ is the renormalised kicking strength and $\alpha = \omega\tau$ is once again the ratio between the period of the kicks and the period of the oscillator. Again we make the choice of $\alpha = 2\pi/q$.

In Fig. 2.4a, we show a plot of Eq. (2.5) for a small value of L, which clearly shows qualitatively different dynamics to the stochastic web for $L = 6$ in Fig. 2.4b. For small L, the orbit decomposes into identical star shapes (sometimes called *supertiles* in the literature [44]) and is unbounded. This is qualitatively different behaviour to Eq. (2.4) with a small kick strength.

For L large enough to ensure a positive maximum LE, we see a growing fractal (with $D_{\mathrm{KY}} \approx 1.78$) that is structurally different to the web we had before in Fig. 2.1a. However, the q-fold rotational symmetry is present in all cases. Irrational choices of q produce a similar picture to Fig. 2.1b. For sufficiently large L, the trajectories are again unbounded for both rational and irrational q.

We plot the LE for Eq. (2.5) in Fig. (2.5). The fact that the LE increases more rapidly than in (2.4) leads to a faster onset of the disordered behaviour mentioned in Chapter 2.1.1 as L gets larger than 4. These results tell us that the motion seen in Fig. (2.4a) is not chaotic according to our definition, although it clearly shows some interesting structure.

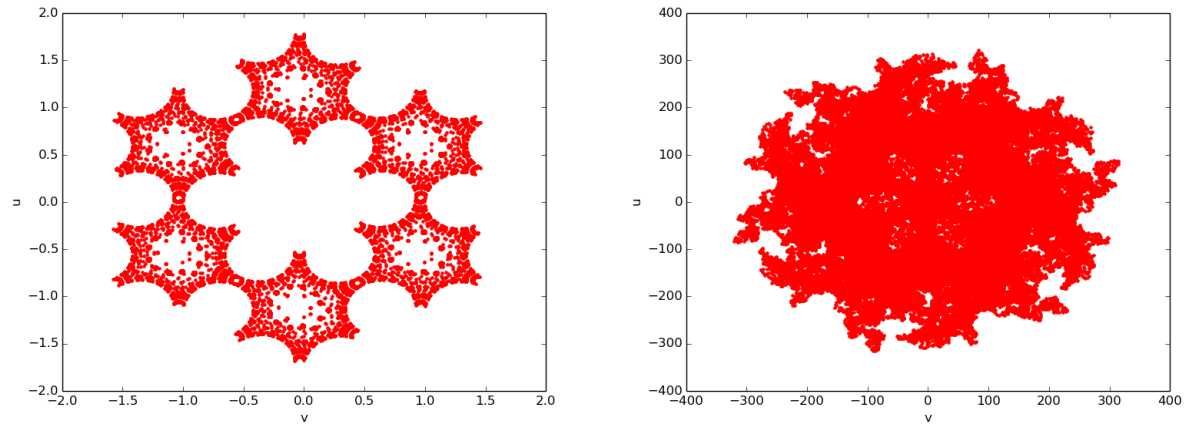

(a) $L = 0.1$. (b) $L = 6$.

Figure 2.4: Plots of the mapping (2.5) for $q = 6$ and different values of L after 10000 kicks. For small choices of L, the dynamics are still largely regular, with regions of stability delineated by the invariant tori. The 'supertiles' tile all of phase space, which we would see if we took n to be larger. For large values of L we get a stochastic web, as for the cosine potential. If we enlarge the central region we see structure that, while still being broadly symmetrical, is much more disordered. As we can see in the right panel, the whole image looks like a branching fractal structure with q-fold rotational symmetry.

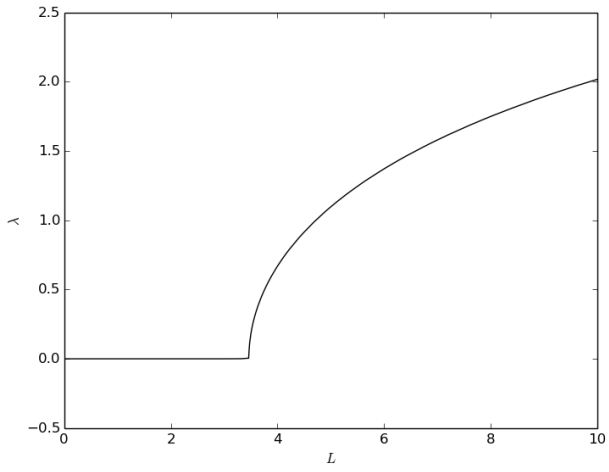

Figure 2.5: Maximum LE λ of (2.5) as a function of L for $q = 6$.

2.2 KAM Theory

We will use a Kolmogorov–Arnold–Moser (KAM) theory approach (though not any particular theorem) to see what behaviour arises in the classical kicked oscillator system when we choose a kick strength that is small enough that the system is not in a chaotic regime. In the literature this is

sometimes called *weak chaos* or *pseudochaos* [28, 44]. This will give us some intutition for how we expect the quantum system to behave in this regime, in particular what effect a choice of small kicking strength (i.e., small enough so that no LE is positive) should have on the breaking time.

KAM theory is concerned with the study of systems of the form

$$H(J,\theta) = H_0(J) + AH_1(J,\theta), \tag{2.6}$$

where A is a parameter, H_0 is an integrable Hamiltonian, H_1 is a nonintegrable Hamiltonian, and J and θ are *action–angle variables* [40]. These variables allow one to determine the frequencies of oscillatory or rotational motion without solving the equations of motion.

For sufficiently large A, the entire system becomes nonintegrable, as the H_1 term dominates. With KAM theory, we study the regime where A is small enough for H_1 to act as a perturbation to the otherwise integrable system. The main concern of KAM theory is with the persistence of quasiperiodic motion under this perturbation [2].

For $A = 0$, the system (2.6) is integrable, so motion is confined by invariant tori in phase space. Hamilton's equations give

$$\begin{aligned}\frac{dJ}{dt} &= \frac{\partial H_0}{\partial \theta} = 0,\\ \frac{d\theta}{dt} &= \frac{\partial H_0}{\partial J} = \nu(J),\end{aligned}$$

so

$$\begin{aligned}J(t) &= J_0,\\ \theta(t) &= \nu(J_0)t + \theta_0,\end{aligned}$$

for the initial conditions J_0 and θ_0. Thus, the motion is confined by a torus of frequency $\nu(J_0)$, where *frequency* refers to the average direction that the orbit moves around the torus. We are interested in the persistence of this invariant torus as we increase A. The KAM theorem of Arnold states that under certain conditions and for a small non-integrable perturbation, the KAM tori of the perturbed system are expected to be similar but distorted versions of the original KAM tori [1].

We now take H_0 to be the harmonic-oscillator Hamiltonian and H_1 to be the kick Hamiltonian:

$$\begin{aligned}H_0 &= \frac{p^2}{2m} + \frac{m\omega^2 x^2}{2},\\ H_1 &= V(x)\sum_{n=-\infty}^{\infty}\delta(t - n\tau).\end{aligned}$$

The invariant tori of the harmonic oscillator are circles, all of which have the same frequency. To apply the formal statement of the KAM theorem in [1] we require that each torus has a different frequency (i.e., the frequencies are *non-degenerate*). This condition is often called the *twist condition*, and it is not met here, so we cannot use the theorem explicitly. However, we can still apply the ideas of KAM theory and, along with some numerical calculations, investigate the breakdown of the KAM tori in a qualitative way.

Consider the cosine potential (1.4). We introduce the action–angle coordinates J and θ using

$$\begin{aligned}x &= \sqrt{\frac{2}{m\omega}}J\cos(\theta),\\ p &= \sqrt{\frac{1}{2m}}J\sin(\theta).\end{aligned}$$

With these coordinates, the Hamiltonian is in the form of (2.6), with

$$\begin{aligned} H_0(J) &= J^2, \\ H_1(J,\theta) &= \cos\left(\sqrt{\frac{2k^2}{m\omega}}J\cos(\theta)\right)\sum_{n=-\infty}^{\infty}\delta(t-n\tau). \end{aligned} \tag{2.7}$$

Note that the action variable J corresponds directly to the radius of the orbits of the harmonic oscillator and hence to the invariant tori of its phase space.

The cosine term in H_1 can be replaced by its series expansion to give

$$H_1(J,\theta) = \sum_{l=0}^{\infty}\left(\frac{-2k^2J^2}{m\omega_\delta}\right)^l\frac{\cos^{2l}(\theta)}{(2l)!}\sum_{n=-\infty}^{\infty}q^l\delta(t-n\tau), \tag{2.8}$$

where we have introduced $\omega_\delta = 2\pi/\tau$, so $q = \omega_\delta/\omega$ is the ratio between the two frequencies of the system, the same as in Chapter 2. We can express Eq. (2.8) in the more readable form

$$H_1(J,\theta) = \sum_{l=0}^{\infty}(-1)^l f_l(J,\theta,\omega_\delta)\sum_{n=-\infty}^{\infty}g_{ln}(\omega_\delta,q),$$

where

$$\begin{aligned} f_l(J,\theta,\omega_\delta) &= \left(\frac{-2k^2J^2}{m\omega_\delta}\right)^l\frac{\cos^{2l}(\theta)}{(2l)!}, \\ g_{ln}(\omega_\delta,q) &= q^l\delta(t-n\tau). \end{aligned}$$

In Eq. (2.8), it is the relationship between the frequencies ω and ω_δ that is paramount. The function $g_{ln}(\omega_\delta,q)$ depends on q and hence gives a way of seeing the effect of the choice of q has on the existence of resonant frequencies in the complete system. Indeed, we can see from Eq. (2.8) that in addition to the frequency ω_δ, the cosine term is sampled at infinitely many other resonant frequencies $\omega_l = \omega^{-l}$, and it is these resonances that cause the breakdown of the tori in phase space. KAM theory indicates that only tori with sufficiently irrational frequencies will survive under perturbation.

Note from Eq. (2.8) that the kick term can be described by only the first few terms of this sequence when the argument $J\cos(\theta)$ is small [16]. If we can adequately describe the series by its first few terms, the number of resonances ω_l that come in to play is small. As we have identified J with the orbits of the unperturbed system, we can predict that tori centred around the origin and around the period-q fixed points (which can be translated to the origin [16]) will survive the longest under perturbation, as the contribution from the non-integrable term is small in this region. Observe the effect of a small kick strength in Fig. 2.6a, where the circular KAM tori around the origin remain but have been deformed.

In regions of phase space away from the fixed points, more terms are needed to approximate H_1, so the number of resonant frequencies involved grows, leading to a breakdown of the tori.

As A grows, the regions around the fixed points contract. The resonances cause some tori to break and the rest to distort, leading to regions of chaotic behaviour forming around the distorted tori and finally to the stochastic web that we observed in Fig. 2.1. We can see this beginning to

occur in Fig. 2.6b, where the orbit of the point (2,2), coloured pink in the figure, is no longer constrained by invariant tori and instead spreads across phase space in the gaps between the remaining tori.

As some integrable structures remain for small A, we expect that the quantum system will show a better correspondence with the classical system than in the case of large A. We investigate this further in Chapter 3.

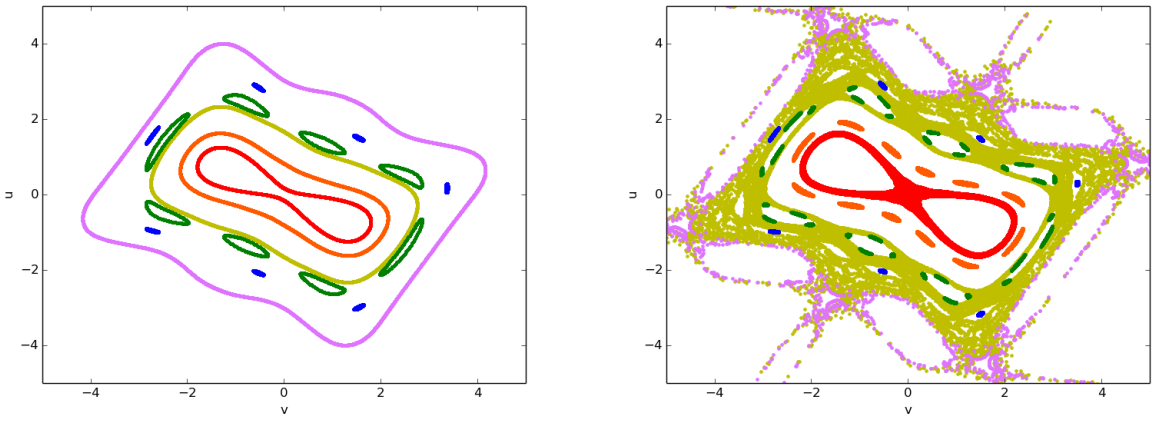

(a) $K = 1.5$.

(b) $K = 1.7$.

Figure 2.6: Plots of the cosine potential mapping (2.4) for $q = 6$ and two values of K. Each colour corresponds to the orbit of a different initial condition. It is clear from these images that the invariant tori of the harmonic oscillator persist under small enough perturbations, albeit with some deformation. As K increases, the tori further out from the fixed points and cycles break down, leading to chaotic dynamics.

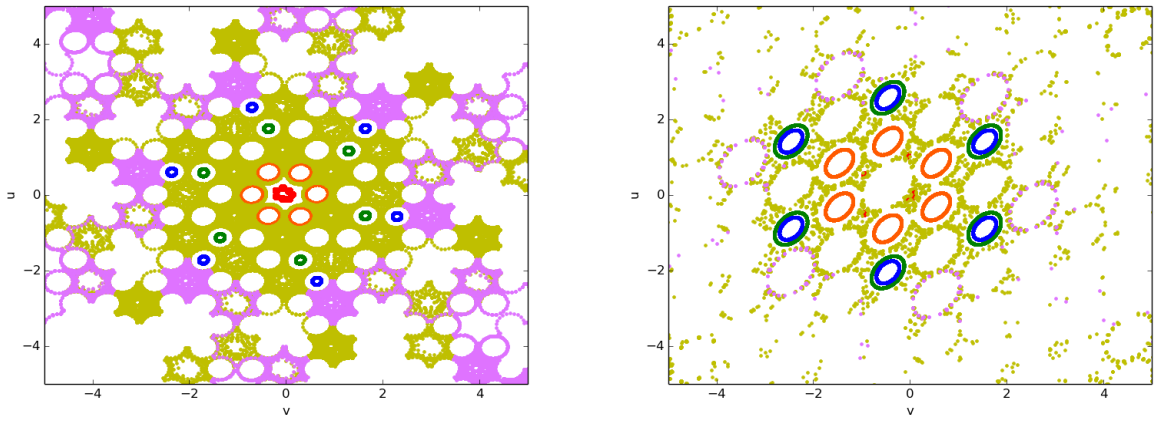

(a) $L = 0.1$.

(b) $L = 1$.

(c) $L = 2$.

(d) $L = 3$.

Figure 2.7: Plots of the sawooth potential mapping (2.5) for $q = 6$ and different values of L, where each colour corresponds to the orbit of a different initial condition. This potential has more interacting frequencies and less symmetry than the cosine potential, which leads to more complex dynamics. Panel (a) shows that tori around the q-cycles persist under small perturbations and that the chaotic motion is still constrained by regions of integrability. As L increases, the tori stretch into ellipses and eventually break, which we can see occuring in (b) and (c). Some remain even under fairly large perturbations, as we can see in (d).

2.3 A Dissipative Environment

Classically, we will model a dissipative environment by introducing a damping term proportional to the velocity, so between the kicks the system evolves according to

$$\ddot{x} + \omega^2 x + \Gamma \dot{x} = 0, \tag{2.9}$$

where $\Gamma > 0$ is the dissipation rate. This is not the only way of incorporating dissipation into the model, but it is the simplest and models a real-world situation, that of the oscillator undergoing friction.

We can then derive a form of Eq. (2.2) that incorporates dissipation:

$$\begin{aligned} x_{n+1} &= e^{-\Gamma\tau/2}(x_n \cos(\bar{\alpha}) + \frac{\sin(\bar{\alpha})}{m\Omega}[p_n - AV^{'}(x_n)]), \\ p_{n+1} &= e^{-\Gamma\tau/2}([p_n - AV^{'}(x_n)]\cos(\bar{\alpha}) - x_n m\Omega \sin(\bar{\alpha})), \end{aligned} \tag{2.10}$$

where

$$\begin{aligned} \Omega &= \sqrt{\omega^2 - \Gamma^2/4}, \\ p_n &= m(\dot{x}_n + \Gamma x_n/2), \\ \bar{\alpha} &= \Omega\tau. \end{aligned} \tag{2.11}$$

This is similiar to Eq. (2.2), but with a new oscillator frequency Ω and the addition of an exponential decay term. Previously the kick mapping depended on two free parameters, but it now also depends on a third, the dissipation rate Γ.

2.3.1 Cosine Potential

As before, we switch to dimensionless variables

$$\begin{aligned} \bar{v} &= kx, \\ \bar{u} &= \frac{kp}{m\Omega}, \end{aligned}$$

and a nondimensionalised form of Eq. (2.10)

$$\begin{aligned} \bar{v}_{n+1} &= e^{-\Gamma\tau/2}(\bar{v}_n \cos(\bar{\alpha}) + \sin(\bar{\alpha})[\bar{u}_n + \bar{K}\sin(\bar{v}_n)]), \\ \bar{u}_{n+1} &= e^{-\Gamma\tau/2}([\bar{u}_n - \bar{K}\sin(\bar{v}_n)]\cos(\bar{\alpha}) + \bar{v}_n \sin(\bar{\alpha})), \end{aligned} \tag{2.12}$$

where $\bar{K} = Ak^2/(m\Omega)$ is the new dimensionless kick strength and $\bar{\alpha} = \Omega\tau$ plays the same role as before.

In Fig. 2.8 we see that the introduction of the dissipative environment has destroyed the stochastic web we observed in the system without a reservoir. In fact, the fixed points of the conservative system have become strange attractors, with $D_{\mathrm{KY}} \approx 1.62$ [19]. The crystal symmetry is also no longer present, and numerical experiments for several values of $\Gamma\tau/2$ that give rise to an attractor do not seem to be different for rational versus irrational choices of q.

In Fig. 2.9a we show the maximum LE as a function of Γ, with $\bar{K}$ and q held constant. Observe that there are now interleaved regions of chaotic and non-chaotic dynamics unlike in Fig. 2.2, which shows only chaotic dynamics after a certain value of K. We show the bifurcation diagram for u in Fig. 2.9b. We observe a cascade of period-doubling bifurcations which occur when changes in the parameter lead to the system switching to a new behavior with twice the period of the original system. Such bifuractions are seen in many chaotic maps, most famously the logistic map [45].

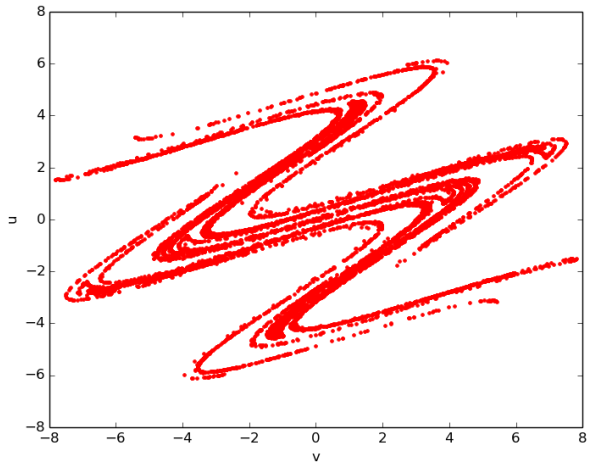

Figure 2.8: The attractor that results from plotting Eq. (2.12) with $\bar{K} = 6$, $\Gamma\tau/2 = 0.36$, and $q = 6$ after 10000 kicks.

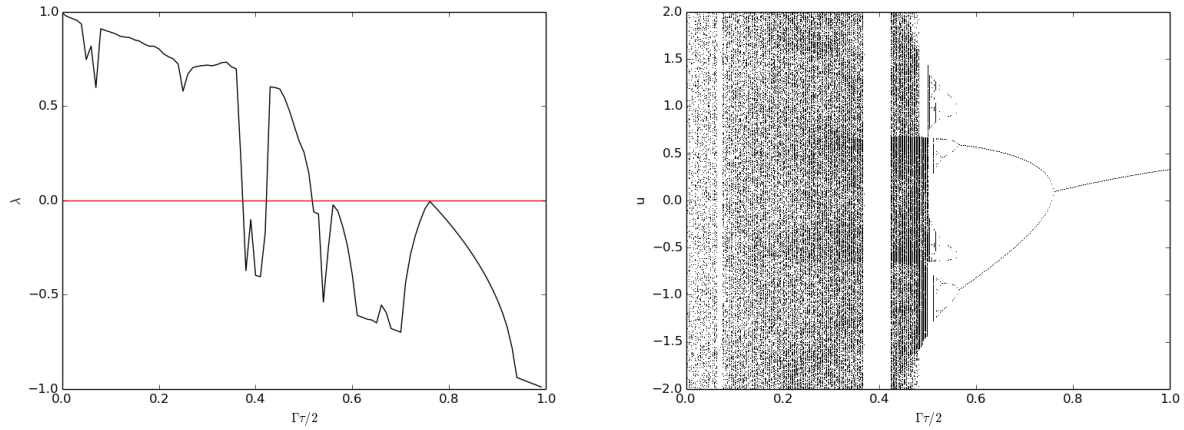

(a) LE.

(b) Bifurcation diagram.

Figure 2.9: (a) Maximal LE λ as a function of $\Gamma\tau/2$ for $\bar{K} = 6$ and $q = 6$. For each value of $\Gamma\tau/2$, we calculate the exponent along a single trajectory by iterating the map 10^5 times, calculating the separation of nearby points at each step, and then averaging to obtain an approximate λ. We then average these over 10^5 trajectories with initial points chosen uniformly from around the origin. (b) Bifurcation diagram for the system. The vertical axis corresponds to 10^3 iterates of u after the first 10^5 transients have been discarded. We show only $u \in [-2, 2]$ for clarity.

2.3.2 Sawtooth Potential

We nondimensionalise with

$$\bar{v} = \frac{x}{\kappa},$$
$$\bar{u} = \frac{p}{m\Omega\kappa},$$

to obtain the kick-to-kick mapping

$$\begin{aligned}\bar{v}_{n+1} &= e^{-\Gamma\tau/2}(\bar{v}_n\cos(\bar{\alpha}) + \sin(\bar{\alpha})[\bar{u}_n + \bar{L}(\lfloor\bar{v}_n\rfloor - \bar{v}_n)]),\\ \bar{u}_{n+1} &= e^{-\Gamma\tau/2}([\bar{u}_n + \bar{L}(\lfloor\bar{v}_n\rfloor - \bar{v}_n)]\cos(\bar{\alpha}) - \bar{v}_n\sin(\bar{\alpha})),\end{aligned} \tag{2.13}$$

where $\bar{L} = A/(m\Omega)$ is the dimensionless kick strength.

In the open system, we observe a sharp difference between the sawtooth and cosine potentials. In Fig. 2.10a, we see the strange attractor (with $D_{\mathrm{KY}} \approx 1.17$) takes a completely different form to that shown in Fig. 2.8. The bifurcation diagram in Fig. 2.10b illustrates that the effect of dissipation is to constrain motion in phase space, with higher values eventually forcing all trajectories to a fixed point. This is a clear contrast with the case of the cosine potential, where we saw that the system exhibits period-doubling bifurcations.

For small L, even small Γ destroys the structure observed in Fig 2.7a. Again, all trajectories go to a fixed point.

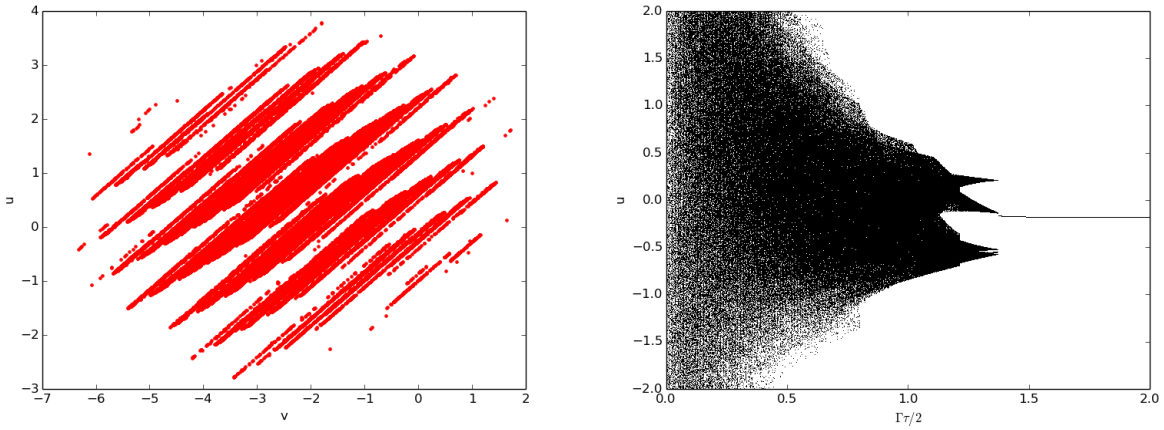

(a) Attractor.

(b) Bifurcation diagram.

Figure 2.10: (a) Plot of Eq. (2.13) with $\bar{L} = 6$, $q = 6$ and $\Gamma\tau/2 = 0.36$. (b) Bifurcation diagram for the system. As in Fig. 2.9b, the vertical axis corresponds to 10^3 iterates of u after the first 10^5 have been discarded, and we show only $u \in [-2, 2]$ for clarity.

3 Quantum Dynamics of the Closed System

3.1 The Quantum Delta-Kicked Oscillator

We quantise the kicked oscillator system by replacing the classical observables x and p in Eq. (1.3) by their quantum analogues, the operators $\hat{x}$ and $\hat{p}$ defined by

$$\hat{x}\,|\psi(x)\rangle = x\,|\psi(x)\rangle\,,$$
$$\hat{p}\,|\psi(x)\rangle = -i\hbar\frac{\partial}{\partial x}\,|\psi(x)\rangle\,.$$

It is convenient to express the quantised Hamiltonian $\hat{H}$ in terms of the harmonic oscillator creation operator

$$\hat{a} = \hat{x}\sqrt{\frac{m\omega}{2\hbar}} + i\hat{p}\sqrt{\frac{1}{2m\hbar\omega}},$$

and its adjoint $\hat{a}^\dagger$. The Schrödinger equation is then [24]

$$i\hbar\frac{d}{dt}\,|\psi\rangle = \left[\hbar\omega\left(\hat{a}^\dagger\hat{a} + \frac{1}{2}\right) + AV\left(\sqrt{\frac{\hbar}{2m\omega}}(\hat{a}^\dagger + \hat{a})\right)\sum_{n=-\infty}^{\infty}\delta(t - n\tau)\right]|\psi\rangle\,. \tag{3.1}$$

We apply Floquet theory [31], a technique for handling differential equations with periodic coefficients, to Eq. (3.1) to derive an equation for the evolution of the wave function. Analogously to the classical case, we immediately arrive at the equation for the time evolution of the wave function between kicks:

$$|\psi(t)\rangle = e^{-i(\hat{a}^\dagger\hat{a}+1/2)\omega t}\,|\psi(0)\rangle\,.$$

To take the kicks into account, we integrate over an infinitesimal interval around each kick, leading to the Floquet operator for the system, which maps the wave function from the moment before a kick to the moment before the next one:

$$\hat{F} = e^{-i(\hat{a}^\dagger\hat{a}+1/2)\alpha}e^{-iA_qV(\sqrt{(\hbar/2m\omega)}[\hat{a}^\dagger+\hat{a}])}, \tag{3.2}$$

where $\alpha = \omega\tau = 2\pi/q$ as in the classical system and $A_q = A/\hbar$ is the quantum kick strength.

3.2 The Semiclassical Limit

Our primary interest is in the semiclassical limit $\hbar \to 0$, so we will consider $\hbar$ as an additional parameter of our system. For both the cosine and sawtooth potentials, we can find a dimensionless *effective* $\hbar_{\text{eff}}$ (we also call this a *classicality parameter*), which is the ratio between the true $\hbar$ and a typical action of the system. We consider the limit $\hbar_{\text{eff}} \to 0$.

We define $\hbar_{\text{eff}}$ so that it is dimensionless and dependent on other parameters of the system. This allows us to vary it in experiments, which we cannot realise with $\hbar$, which is constant. This makes it attractive, as it allows us to confirm our analysis experimentally.

3.3 The Phase-Space Formulation of Quantum Mechanics

We wish to study how the dynamics of (3.2) change as we adjust a parameter, e.g. whether there is a difference between rational and irrational choices of q. Classically, we often do this by following a single trajectory to explore phase space and its structures, as in Chapter 2. In the associated quantum system this is impossible for us to do, as the uncertainty principle prevents one from defining a single trajectory. Instead, we attempt to link the wave function to a probability distribution in phase space, an idea that was pursued independently by several early quantum theorists but most famously by Herman Weyl and Eugene Wigner [55].

This approach is intutive if we consider a probabilistic formulation of classical mechanics. Quantum mechanics is linear, which seems to pose a problem when dealing with classical nonlinear systems, but even for nonlinear systems the classical probability distribution still evolves in a linear fashion according to Liouville's equation

$$\frac{\partial \rho}{\partial t} = \{H, \rho\}, \tag{3.3}$$

and in this sense all of classical mechanics is also linear.

The tool that we use in the quantum regime is the *Wigner function*, introduced by Wigner in [55]. Consider a quantum system with Hamiltonian $\hat{H}$ in a state given by the density operator $\hat{\rho}$. The Wigner function for the system is defined by

$$\mathcal{W}(\beta, \beta^*) = \frac{1}{\pi^2} \int e^{\lambda^* \beta - \lambda \beta^*} e^{-|\lambda|^2/2} \chi(\lambda, \lambda^*) d^2\lambda \tag{3.4}$$

where $\beta = x + ip$ for suitably rescaled position x and momentum p [23]. The *characteristic function* χ is given by

$$\chi(\lambda, \lambda^*) = \mathbf{Tr}[\hat{\rho} e^{\lambda \hat{a}^\dagger - \lambda^* \hat{a}}], \tag{3.5}$$

where **Tr** is the operator trace. This function arises in the study of *quantum characteristics*, which are phase space trajectories that arise from the Wigner transform of the operators $\hat{x}$ and $\hat{p}$ [53].

The distribution is real-valued and behaves as a joint distribution for x and p, two of the axioms for probability distributions. Strictly speaking, $\mathcal{W}$ is only a quasiprobability distribution as it dos not obey the third axiom: it can take on negative values. We call these regions of negative probability *quantum interference*. From a physical perspective, there interference regions correspond to parts of phase space that are classically forbidden. The uncertainty principle ensures that these regions are small (i.e., are contained within compact sets of radius $O(\hbar)$) and hence disappear in the classical limit.

The Wigner function evolves according to the equation

$$\begin{aligned} \frac{\partial \mathcal{W}}{\partial t} &= \{\{\hat{H}, \mathcal{W}\}\}_{MB} \\ &= \{\hat{H}, \mathcal{W}\} + \sum_{n=0}^{\infty} \frac{(-1)^n \hbar^{2n}}{2^{2n}(2n+1)!} \frac{\partial^{2n+1} \mathcal{W}}{\partial x^{2n+1}} \frac{\partial^{2n+1} \mathcal{W}}{\partial p^{2n+1}}, \end{aligned} \tag{3.6}$$

where $\{\{.,.\}\}_{MB}$ is the Moyal bracket [47] and $\{.,.\}$ is the classical Poisson bracket. Equation (3.6) is similar to the Liouville equation (3.3) for the evolution of a classical PDF, but there is also a quantum correction.

The Wigner function (3.4) encodes the entire state of a system [57]. Hence when taken alongside its evolution equation (3.6) it forms the basis of a complete formulation of quantum mechanics, often called the *phase-space formulation* [4]. This formulation does not rely on a Hilbert space or on observables, and is hence attractive for discussing comparisons between classical systems and their quantum counterparts.

An alternative to the Wigner function is the *Husimi distribution* (i.e., Q-function [33]), which can be obtained from the Wigner distribution by applying a Weierstrass transform (local smoothing via a Gaussian filter [59]). We have looked at plots of the Husimi distribution for the kicked oscillator, but do not include them here.

3.4 Cosine Potential

Recall the cosine potential $V(x) = \cos(kx)$. In this case, the Floquet operator is

$$\hat{F} = e^{-i(\hat{a}^\dagger \hat{a} + 1/2)\alpha} e^{-iK_q \cos(\eta[\hat{a}^\dagger + \hat{a}])}, \tag{3.7}$$

where we have introduced the *Lamb–Dicke parameter*

$$\eta = k\sqrt{\frac{\hbar}{2m\omega}}. \tag{3.8}$$

The Lamb–Dicke parameter is the classicality parameter for the kicked oscillator with the cosine potential. Equation (3.7) has three parameters: K, α, and η. This contrasts with the classical evolution in Eq. (2.4), which depends only on the first two. No change of variables is going to remove the dependence on η. Note that we can write the kick strength in terms of this parameter: $K_q = K/(2\eta^2)$.

In Fig. 3.1 we show the Wigner functions for the kicked oscillator for two values of η. We observe better correspondence with the classical structure shown in Fig. 2.3a as we reduce η, though regions of quantum interference are still present.

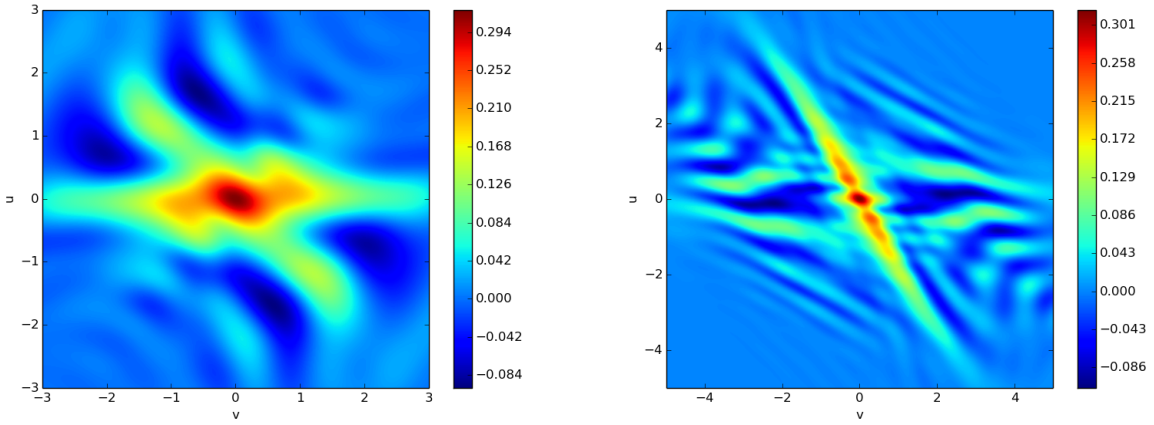

(a) $\eta = 0.5$. (b) $\eta = 0.25$.

Figure 3.1: Wigner functions for the kicked oscillator with the cosine potential, with parameter values $K = 2$ and $q = 6$ after 9 kicks, for different choices of η. We generated these using the QuTiP library for Python [35], which provides methods for computing the matrices of operators and Wigner functions. We used a Hilbert Space of dimension 2^8, and the initial state is a coherent state centred at the origin (i.e., $|0\rangle$, the ground state of the harmonic oscillator). We plot the Wigner function on a $10^3 \times 10^3$ grid.

If we choose comparable initial conditions, then initially the classical and quantum systems are identical. Classically we consider a normal distribution centred at the origin and with variance 1. This has PDF

$$f(x) = \frac{1}{\sqrt{2\pi}} e^{-x^2/2}.$$

The comparable quantum state is a coherent state centred at the origin; this has wave function

$$f(x) = \frac{1}{\sqrt{2\pi}} e^{-m\omega x^2/2\hbar},$$

up to a normalisation constant. Note that we can translate the classical normal distribution so that it is centred at any point, and that similarly we can translate the coherent state to get one centred at any point.

As time goes on, nonlinearities in the potential become important and cause a breakdown of quantum–classical correspondence. The time at which this breakdown first occurs is the *breaking time*, which we can estimate using the characteristic function (3.5).

Let $|\psi_n\rangle$ be the state vector for the system just before the nth kick. Substituting the density operator $\hat{\rho}_n = |\psi_n\rangle \langle\psi_n|$ into Eq. (3.5) and taking the trace, we obtain the following expression for the characteristic function after n kicks:

$$\begin{aligned} \chi_n(\lambda, \lambda^*) &= \langle\psi_n| e^{\lambda \hat{a}^\dagger - \lambda^* \hat{a}} |\psi_n\rangle \\ &= \langle\psi_{n-1}| \hat{F}^\dagger e^{\lambda \hat{a}^\dagger - \lambda^* \hat{a}} \hat{F} |\psi_{n-1}\rangle . \end{aligned} \tag{3.9}$$

We substitute the Floquet operator into (3.9) and expand the exponential in terms of Bessel functions J_m. We use the Jacobi–Anger expansion

$$e^{iz\sin(\phi)} = \sum_{m=-\infty}^{\infty} J_m(z)e^{im\phi}, \tag{3.10}$$

to obtain a recurrence relation for χ_n, which in turn gives us an expression for the characteristic function (3.5) in terms of the initial value C_0.

$$\chi_n(\lambda, \lambda^*) = \sum_{m_1,\ldots,m_n=-\infty}^{\infty} J_{m_1}(z_1)\ldots J_{m_n}(z_n)C_0(\lambda_n, \lambda_n^*), \tag{3.11}$$

where

$$\begin{aligned} \lambda_k &= \lambda_{k-1}e^{i\alpha} + im_k\eta, \\ z_k &= 2K_q\sin(\mu_k), \\ \mu_k &= -\frac{\eta}{2}(\lambda_k + \lambda_k^*), \\ \lambda_0 &= \lambda. \end{aligned} \tag{3.12}$$

The full proceedure for this is given in [22]. We omit the details here, and will give a variation on the full argument for the sawtooth potential in Chapter 3.5, as it is a new calculation.

To estimate the breaking time, we compare Eq. (3.11) with its classical analogue. The classical expression for the characteristic function is

$$\chi_n^{\text{class}}(\lambda, \lambda^*) = \iint \rho e^{\lambda a^* - \lambda^* a} d\lambda d\lambda^*$$

for a classical PDF ρ and a complex number a. The classical formula is almost identical to (3.11):

$$\chi_n^{\text{class}}(\lambda, \lambda^*) = \sum_{m_1,\ldots,m_n=-\infty}^{\infty} J_{m_1}(K\mu_1/\eta^2)\ldots J_{m_n}(K\mu_n/\eta^2)C_0(\lambda_n, \lambda_n^*), \tag{3.13}$$

where μ_k is as in Eq. (3.12). Because $2K_q = K/(\eta^2)$, these expressions are similar when $\sin(\mu_k) \approx \mu_k$ (i.e., when $|\mu_k| \ll 1$). From Eq. (3.12), we know that $\mu_k \propto \eta$, so for small values of η we have $|\mu_k| \ll 1$, and there is good correspondence between the classical and quantum predictions. Eventually λ_k grows large enough to cause this correspondence to break down.

The time at which this breakdown occurs is the breaking time $t_\hbar$. When $|K\sin(\alpha) \gg 1|$, it was shown in [22] that

$$t_\hbar \approx \frac{\ln(2K/\eta)}{\ln(K\sin(\alpha))}, \tag{3.14}$$

When $|K\sin(\alpha) \ll 1|$, the breaking time takes the form

$$t_\hbar \approx \frac{1}{K\eta^2}, \tag{3.15}$$

We can support these results for the breaking time with numerical computations. To do this, we require an appropriate notion of a 'distance' between quantum and classical systems. One choice

is to compare the Wigner function with the classical PDF using Eq. (3.6). By comparing the magnitutes of the Moyal and Poisson brackets, we obtain an estimate for the size of the quantum correction. However, this presents problems both in terms of the computational cost and also the experimental difficulty of resolving narrow interferences fringes in the Wigner function.

For our purposes, it is simpler to consider the relative distance between the variances in the quantum ($\Delta_q^2 v$) and classical ($\Delta_{cl}^2 v$) distributions:

$$d_r = \left| \frac{\Delta_q^2 v - \Delta_{cl}^2 v}{\Delta_{cl}^2 v} \right|. \tag{3.16}$$

Although the variance is far from a complete characterisation of the distributions, this simple measure already shows the scaling behaviour predicted above (see Fig. 3.3). Other possible measures include the von Neumann entropy [52] and the Kullback–Liebler distance [5].

The annihilation operator is $\hat{a} = (\hat{v} + i\hat{u})/(2\eta)$, where $\hat{v}$ and $\hat{u}$ are the rescaled position and momentum operators that correspond to the dimensionless quantities (2.3). To ensure we use the same scale for the classical and quantum systems, we use the substitution $(v, u) \mapsto (v, u)/(2\eta)$ to introduce η into the map (2.4).

Numerically, we exhibit the breaking time as the first time for which d_r exceeds some threshold value ϵ, which we have chosen to be 0.1. In Fig. 3.2a, we consider $K = 2$ and plot d_r for two different values of η. As we expect, the distance d_r stays below ϵ for a longer time when η is smaller. In Fig. 3.2b, we show the results for $K = 0.5$. As our expression for the breaking time predicts the quantum–classical correspondence stays good for much longer and the distance d_r grows very slowly.

In Fig. 3.3, we plot the values of breaking time obtained through this method versus Eq. (3.14) for $K = 2$ and Eq. (3.15) for $K = 0.5$ to check whether our analytical expressions do in fact have the predicted scaling behaviour. Despite the oscillations in the plots, they both show some agreement with the analytical predictions.

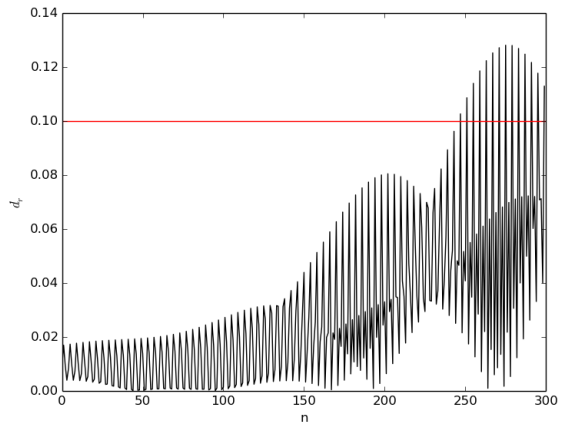

(a) $K = 0.5$.

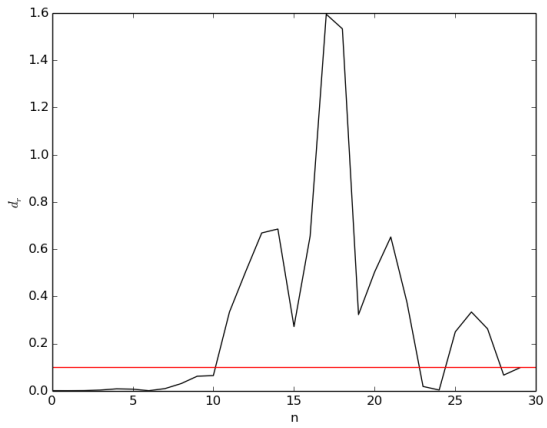

(b) $K = 2$.

Figure 3.2: Plots of Eq. (3.16) with (a) $K = 0.5$ and (b) $K = 2$ for $q = 6$ and $\eta = 0.1$. Observe that for $K = 2$ the breaking time is fairly short as expected, with $t_\hbar \approx 10$ kicks. For small values of η the breaking time is very long, with $t_\hbar \approx 250$ for $K = 0.5$. This agrees with both our analytical result (3.15) and the intuition from KAM theory (see Chapter 2.2) that the associated classical system is close to being integrable.

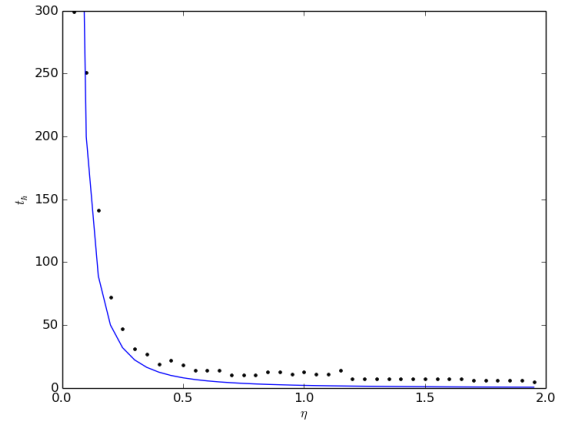

(a) $K = 0.5$.

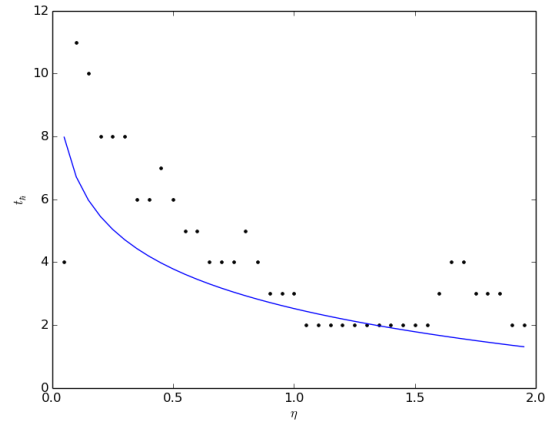

(b) $K = 2$.

Figure 3.3: Breaking time as obtained analytically (blue curve) and numerically using Eq. (3.16) (points) for two values of K. For $K > 1$, the numerical predictions show similar scaling behaviour to the analytic predictions, although there are some oscillations. For $K < 1$ we observe a good correspondence between the two results.

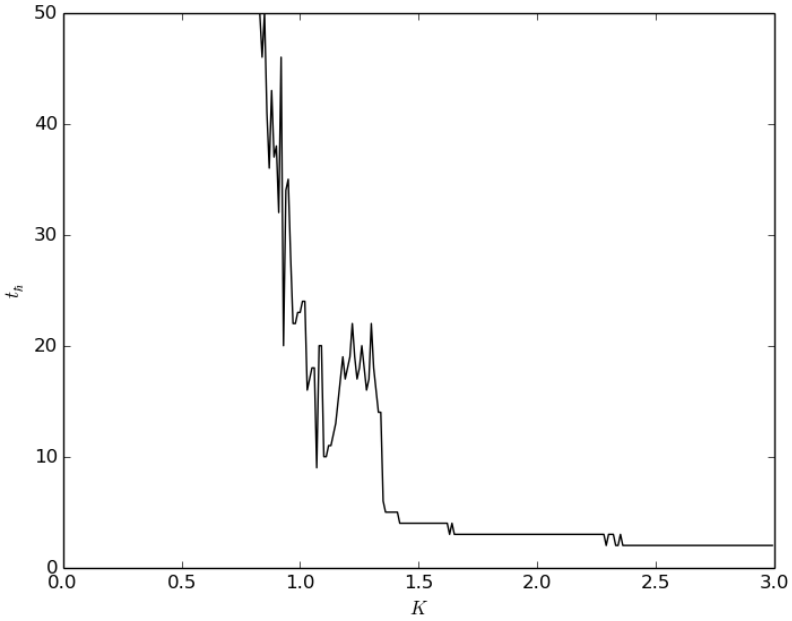

Figure 3.4: Plots of the breaking time $t_\hbar$ using the diagnostic (3.16) for a fixed value of $\eta = 0.1$ and different values of K. We cut off the graph at $t_\hbar = 50$ for clarity. Observe that the breaking time grows rapidly as $K \to 0$, as we expect. There is a rapid drop in breaking time as $K \to 1$. This agrees with the KAM theory discussion in Chapter 2.2 that suggests that the dynamics near the origin becomes increasingly non-integrable around this value.

3.5 Sawtooth Potential

Recall the sawtooth potential (1.5):

$$V(x) = \frac{\kappa x}{2} + \frac{\kappa^2}{2\pi^2} \sum_{j=1}^{\infty} \frac{1}{j^2} \cos\left(\frac{2j\pi x}{\kappa}\right).$$

Substituting Eq. (1.5) into Eq. (3.2) yields the Floquet operator

$$\hat{F} = e^{-i(\hat{a}^\dagger \hat{a} + 1/2)\alpha} e^{-iL_q \sigma(\hat{a}^\dagger + \hat{a})/2} e^{-iL_q \sum_{j=1}^{\infty} \hat{G}_j}, \tag{3.17}$$

where we have introduced the operators

$$\hat{G}_j = \frac{1}{\pi j^2} \cos(j\sigma[\hat{a}^\dagger + \hat{a}]), \qquad j = 1, 2, 3, ...$$

the classicality parameter

$$\sigma = \frac{\pi}{\kappa} \sqrt{\frac{2\hbar}{m\omega}},$$

and the quantum kick strength

$$\begin{aligned} L_q &= \frac{A\kappa^2}{2\pi\hbar} \\ &= \frac{\pi L}{\sigma^2}. \end{aligned}$$

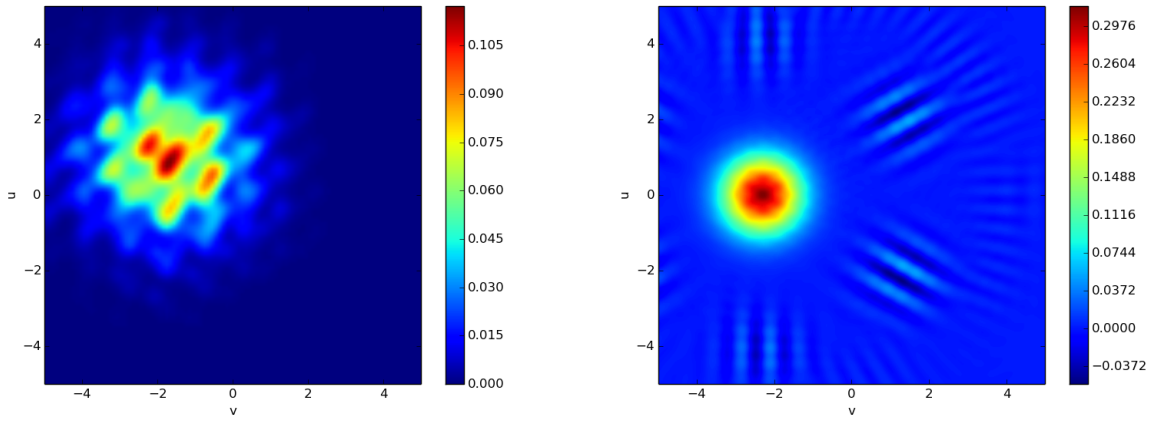

Figure 3.5: (Left) PDF for the kicked oscillator with the sawtooth potential after 9 kicks for $L = 6$ and $q = 6$. (Right) Wigner distribution for the associated quantum system with the same parameters and $\sigma = 0.1$. We observe many differences between the quantum and classical distributions even for this low value of σ. For example, the quantum distribution is centred at approximately $(-2, 0)$, whereas the classical distribution is closer to $(-1.7, 0.5)$.

Once again, we estimate the breaking time by comparing the quantum characteristic function in Eq. (3.5),

$$\chi(\lambda, \lambda^*) = \mathbf{Tr}[\hat{\rho} e^{\lambda \hat{a}^\dagger - \lambda^* \hat{a}}],$$

with its classical counterpart

$$\chi_n^{\text{class}}(\lambda, \lambda^*) = \iint \rho e^{\lambda a^* - \lambda^* a} d\lambda d\lambda^*$$

To do this we proceed as outlined in Chapter 3.4, by substituting the Floquet operator into the characterisitic function $\chi(\lambda, \lambda^*)$ and expanding the result to obtain an expression in terms of Bessel functions that can easily be compared to the classical expression.

The infinite sum in the Floquet operator (3.17) poses a problem, so we approximate it by only considering the first M terms:

$$\hat{F}_M = e^{-i(\hat{a}^\dagger \hat{a} + 1/2)\alpha} e^{-iL_q \sigma(\hat{a} + \hat{a}^\dagger)/2} e^{-iL_q \sum_{j=1}^{M} \hat{G}_j}. \tag{3.18}$$

This is justified by the observation that for sufficiently large j, the entires in the matrix of $\hat{G}_j$ (when we consider a finite dimensional Hilbert space for the system with the basis of eigenstates of the harmonic oscillator) are very small, and hence contribute little to the sum. This can be shown numerically, and implies that for large M, $\hat{F}_M \approx \hat{F}$.

Substituting Eq. (3.18) into Eq. (3.5) and applying the relations

$$\begin{aligned} e^{t\hat{a}^\dagger \hat{a}} f(\hat{a}, \hat{a}^\dagger) e^{-t\hat{a}^\dagger \hat{a}} &= f(\hat{a} e^{-t}, \hat{a}^\dagger e^{t}), \\ e^{-t\hat{a}^\dagger} f(\hat{a}, \hat{a}^\dagger) e^{t\hat{a}^\dagger} &= f(\hat{a} + t, \hat{a}^\dagger), \\ e^{t\hat{a}} f(\hat{a}, \hat{a}^\dagger) e^{t\hat{a}} &= f(\hat{a}, \hat{a}^\dagger + t), \end{aligned} \tag{3.19}$$

we obtain

$$\chi_n(\lambda,\lambda^*) = \langle\psi_{n-1}|\exp\left(iL_q\sum_{j=1}^{M}\hat{G}_j\right)\exp(\lambda e^{i\alpha}\hat{a})\exp(-\lambda^* e^{-i\alpha}\hat{a}^\dagger)\exp\left(-iL_q\sum_{j=1}^{M}\hat{G}_j\right)|\psi_{n-1}\rangle\,, \tag{3.20}$$

where we have also used the fact that the operators $\hat{G}_j$ are self-adjoint. To expand (3.20), we define

$$D_k(\lambda) = \exp\left(iL_q\sum_{j=k}^{M}\hat{G}_j\right)\exp(\lambda e^{i\alpha}\hat{a})\exp(-\lambda^* e^{-i\alpha}\hat{a}^\dagger)\exp\left(-iL_q\sum_{j=k}^{M}\hat{G}_j\right).$$

Because the operators $\hat{G}_j$ commute with one another, we can write

$$\begin{aligned} D_k(\lambda) =& \exp\left(iL_q\sum_{j=k+1}^{M}\hat{G}_j\right)\exp(iL_q\hat{G}_k)\exp(\lambda e^{i\alpha}\hat{a})\exp(-\lambda^* e^{-i\alpha}\hat{a}^\dagger)\exp(-iL_q\hat{G}_k)\ \times \\ & \exp\left(-iL_q\sum_{j=k+1}^{M}\hat{G}_j\right), \end{aligned}$$

which is equivalent to

$$\begin{aligned} D_k(\lambda) =& \exp\left(iL_q\sum_{j=k+1}^{M}\hat{G}_j\right)\exp(\lambda e^{i\alpha}\hat{a})\exp(-\lambda e^{i\alpha}\hat{a})\exp(iL_q\hat{G}_k)\exp(\lambda e^{i\alpha}\hat{a})\ \times \\ & \exp(-\lambda^* e^{-i\alpha}\hat{a}^\dagger)\exp(-iL_q\hat{G}_k)\exp(\lambda^* e^{-i\alpha}\hat{a}^\dagger)\exp(-\lambda^* e^{-i\alpha}\hat{a}^\dagger)\exp\left(-iL_q\sum_{j=k+1}^{M}\hat{G}_j\right). \end{aligned}$$

Again using the orderings (3.19), we obtain

$$\begin{aligned} D_k(\lambda) =& \exp\left(iL_q\sum_{j=k+1}^{M}\hat{G}_j\right)\exp(\lambda e^{i\alpha}\hat{a})\exp\left(i\frac{L_q}{\pi k^2}\cos(k\sigma[\hat{a}^\dagger+\hat{a}+\lambda e^{i\alpha}])\right)\ \times \\ & \exp\left(-i\frac{L_q}{\pi k^2}\cos(k\sigma[\hat{a}^\dagger+\hat{a}-\lambda^* e^{-i\alpha}])\right)\exp(-\lambda^* e^{-i\alpha}\hat{a}^\dagger)\exp\left(-iL_q\sum_{j=k+1}^{M}\hat{G}_j\right). \end{aligned} \tag{3.21}$$

The exponentials of the cosines commute, so we can combine these terms in Eq. (3.21) to obtain

$$D_k(\lambda) = \sum_{s_k=-\infty}^{\infty} J_{s_k}\left(\frac{2L_q}{\pi k^2}\sin\left(\frac{\sigma k}{2}(\lambda e^{i\alpha}-\lambda^* e^{-i\alpha})\right)\right)D_{k+1}(\lambda e^{i\alpha}+is_k k\sigma), \tag{3.22}$$

where we have used the Bessel function expansion (3.10). Iterating Eq. (3.22), we obtain the expression

$$\begin{aligned} D_M(\lambda) &= \sum_{s_1,\ldots,s_M=-\infty}^{\infty} J_{s_1}(z_1)\ldots J_{s_M}(z_M)D_{M+1}(\lambda_M) \\ &= \sum_{s_1,\ldots,s_M=-\infty}^{\infty} J_{s_1}(z_1)\ldots J_{s_M}(z_M)e^{\lambda_M e^{i\alpha}\hat{a}}e^{-\lambda_M^* e^{-i\alpha}\hat{a}^\dagger}, \end{aligned} \tag{3.23}$$

where

$$\begin{aligned}
\lambda_k &= \lambda_{k-1}e^{i\alpha} + is_k\xi_k\sigma, \\
\xi_k &= \xi_{k+M} = k, \\
\mu_k &= \frac{\sigma\xi_k}{2}(\lambda_k + \lambda_k^*), \\
z_k &= \frac{2L_q}{\pi\xi_k^2}\sin(\mu_k), \\
\lambda_0 &= \lambda.
\end{aligned} \tag{3.24}$$

Substituting Eq. (3.23) into Eq. (3.20) yields a recurrence relation for the characteristic function:

$$\chi_n(\lambda,\lambda^*) = \sum_{s_1,\ldots,s_M=-\infty}^{\infty} J_{s_1}(z_1)\ldots J_{s_M}(z_M)C_{n-1}(\lambda_M,\lambda_M^*),$$

which we expand to obtain

$$\chi_n(\lambda,\lambda^*) = \sum_{s_1,\ldots,s_{nM}=-\infty}^{\infty} J_{s_1}(z_1)\ldots J_{s_{nM}}(z_M)C_0(\lambda_{nM},\lambda_{nM}^*), \tag{3.25}$$

where C_0 is the initial value of the characteristic function. We compare Eq. (3.25) with the classical version of this expression [22],

$$\chi_n^{\text{class}}(\lambda,\lambda^*) = \sum_{s_1,\ldots,s_{nM}=-\infty}^{\infty} J_{s_1}\left(\frac{2L\mu_1}{\kappa\xi_1^2\sigma^2}\right)\ \ldots\ J_{s_{nM}}\left(\frac{2L\mu_{nM}}{\kappa\xi_{nM}^2\sigma^2}\right)C_0(\lambda_{nM},\lambda_{nM}^*). \tag{3.26}$$

For Eq. (3.25) and Eq. (3.26) to be comparable, we require $|\sin(\mu_k)|\approx|\mu_k|$ (i.e., $|\mu_k|\ll 1$). Assuming that this condition holds, and taking into account that the Bessel functions are exponentially small when $|s_k|\gg|\mu_k|$, it follows that

$$\begin{aligned}
|s_1| &\approx \frac{L\sin(\alpha)}{\sigma\xi_1}\left|\lambda e^{i\alpha} + \lambda^* e^{-i\alpha}\right|, \\
|s_2| &\approx \frac{L\sin(\alpha)}{\sigma\xi_2}\left|(\lambda e^{2i\alpha} + \lambda^* e^{-2i\alpha}) - 2\xi_1 s_1\sigma\sin(\alpha)\right|, \\
&\vdots \\
|s_{nM}| &\approx \frac{L\sin(\alpha)}{\sigma\xi_n}\left|\lambda e^{nMi\alpha} + \lambda^* e^{-nMi\alpha} - 2\xi_1 s_1\sigma\sin((nM-1)\alpha) - \ldots - 2\xi_{nM-1}s_{nM-1}\sigma\sin(\alpha)\right|.
\end{aligned} \tag{3.27}$$

We first consider the case when $|L\sin(\alpha)|\gg 1$. Higher powers of $L\sin(\alpha)$ will dominate in (3.27), so we have

$$\begin{aligned}
|s_1| &\approx \frac{L\sin(\alpha)}{\sigma\xi_1}, \\
&\vdots \\
|s_{nM}| &\approx \frac{(L\sin(\alpha))^{nM}}{\sigma\xi_n}.
\end{aligned}$$

We can then estimate the magnitude of μ_k to be

$$|\mu_k| \approx \frac{\xi_k^2 \pi}{2L_q} |s_k| = \frac{(L\sin(\alpha))^k \sigma \xi_k}{2L} \tag{3.28}$$

The breaking time is the kick n at which some $\mu_{nk} \approx 1$ for $k \in \{1, \ldots, M\}$. Among the first block of M terms, the largest term is

$$|\mu_M| \approx \frac{(L\sin(\alpha))^M \sigma M}{2L}. \tag{3.29}$$

With our assumption that $|L\sin(\alpha)| \gg 1$ we can see that $|\mu_M| \to \infty$ as $M \to \infty$. Thus, in contrast to the cosine potential, the breaking time is $t_\hbar \approx 1$ kick.

We also examine the case when $|L\sin(\alpha)| \ll 1$. We take $L \ll 1$ and $\sin(\alpha) \approx 1$, as $|\sin(\alpha)| \ll 1$ implies that $|\omega\tau| = |\alpha| \ll 1$, and that the timescale considered (one kick period τ) is significantly less than the period of an oscillation [22]. For simplicity we consider just $\alpha = \pi/2$. From Eq. (3.27), we obtain

$$\begin{aligned}
|s_1| &\approx \frac{L}{\sigma\xi_1}, \\
|s_2| &\approx \frac{L^2}{\sigma\xi_2}, \\
|s_3| &\approx \frac{L}{\sigma\xi_1} + \frac{L^3}{\sigma\xi_3}, \\
&\vdots \\
|s_{2k-1}| &\approx \frac{L}{\sigma\xi_1} + (2k-3)\frac{L^3}{\sigma\xi_3} + O(L^5), \\
|s_{2k}| &\approx \frac{kL^2}{\sigma\xi_1} + O(L^4).
\end{aligned} \tag{3.30}$$

We estimate the magnitude $|\mu_k|$ to be

$$|\mu_k| \approx \begin{cases} mL^2\sigma\xi_3 & k = 2m-1 \\ mL\sigma\xi_2/2 & k = 2m \end{cases}, \tag{3.31}$$

which yields the breaking time

$$t_\hbar \approx \frac{2}{3L\sigma}. \tag{3.32}$$

We study the sawtooth potential numerically, as we did for the cosine potential. If we attempt to compare the classical and quantum distributions using (3.16), we find that for $L \gg 1$ the distibutions do indeed separate after just one kick, even when σ is very small (as Fig. 3.5 suggests). For $L \ll 1$ we observe the predicted $O(\sigma^{-1})$ growth, as can be deduced from Fig. (3.6a). This provides some numerical support for our analysis.

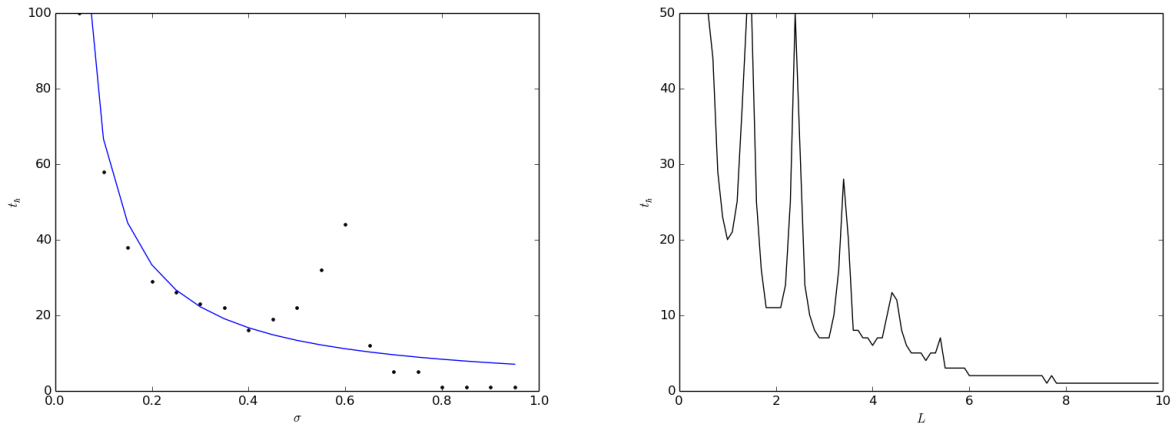

(a) (b)

Figure 3.6: (a) Breaking time for the kicked oscillator with the sawtooth potential as a function of σ with $L = 0.1$ and $q = 6$. The blue line is the analytical prediction, and the black points are the numerical calculations. Apart from the deviation that occurs between 0.4 and 0.6, which is most likely due to the imprecise nature of (3.16), the numerical calculations agree with (3.32). (b) Breaking time as L varies, with $\sigma = 0.1$ fixed, cut off at $t_\hbar = 50$ for clarity. Once again there are oscillations, but we can see that for small L the breaking time is rather high. It plummets as L approaches 4 and finally falls to just 1 kick, consistent with our analysis. The value at which it falls is consistent with Fig. 2.5, which shows the maximum LE becomes positive at roughly the same L, and with Fig. 2.7, which illustrates the persistence of periodic orbits near to the origin for $L = 3$. Our asymptotic analysis is not precise enough to give a description of the breaking time in this parameter regime.

3.6 Localization

We aim to determine the cases in which localization occurs in the kicked oscillator system. Our argument follows [27]. We consider the Floquet eigenstates of the kicked oscillator system (3.2) and put it into the form of a tight-binding model for an electron on a lattice, which we recall from Chapter 1.4 was Anderson's original problem. This approach is independant of the potential V.

The *number basis* $\{|j\rangle\}$ is comprised of eigenstates $|j\rangle$ of the harmonic oscillator Hamiltonian with corresponding eigenenergies $(1/2 + j)\hbar\omega$. In this basis, the Floquet operator (3.2) can be written as

$$\hat{F} = e^{-i\alpha/2} e^{-i\alpha j} e^{-iA_q V(\hat{x})}.$$

The *quasienergy eigenstates* $|\phi\rangle$ of the Floquet operator $\hat{F}$ are then defined by

$$\hat{F}\,|\phi\rangle = e^{-i\Lambda}\,|\phi\rangle\,. \tag{3.33}$$

where the *eigenphase* Λ of the Floquet eigenstate has a corresponding *quasienergy* $\hbar\Lambda$. The existence of these states and that fact that they form a basis is guaranteed by Floquet's theorem [20].

Define a new operator $\hat{W}$ by

$$\hat{W} = -\tan\left[\frac{A_q}{2} V(\hat{x})\right], \tag{3.34}$$

which we can construe as rewriting the kick propogator:

$$e^{-iA_qV(\hat{x})} = \frac{1+i\hat{W}}{1-i\hat{W}}.$$

By substituting Eq. (3.34) into (3.33) we obtain

$$(1+i\hat{W})e^{-i(\alpha(j+1/2)-\Lambda)}\left|\phi\right\rangle = (1-i\hat{W})\left|\phi\right\rangle.$$

We now let $C = \alpha(j+1/2) - \Lambda$ and gather terms on one side to obtain

$$(e^{-iC} - 1 + i\hat{W}e^{-iC} + i\hat{W})\left|\phi\right\rangle = 0. \tag{3.35}$$

We define $\left|\bar{\phi}\right\rangle = (1+e^{-iC})\left|\phi\right\rangle$, with which we can rewrite Eq. (3.35) as

$$\frac{e^{-iC}-1}{e^{-iC}+1}\left|\bar{\phi}\right\rangle + i\hat{W}\frac{e^{-iC}+1}{e^{-iC}+1}\left|\bar{\phi}\right\rangle = 0.$$

We use a standard identity for tan to obtain

$$-i\tan\left(\frac{C}{2}\right) + i\hat{W}\left|\bar{\phi}\right\rangle = 0. \tag{3.36}$$

Dividing Eq. (3.36) by i and introducing $T = -\tan(C/2)$ yields

$$(T+\hat{W})\left|\bar{\phi}\right\rangle = 0.$$

Expanding $\left|\bar{\phi}\right\rangle$ in the number basis $\{\left|j\right\rangle\}$ then gives

$$\begin{aligned}(T+\hat{W})\left|\bar{\phi}\right\rangle &= \sum_{j=0}^{\infty}\left|j\right\rangle\left[\left\langle j\right|T\left|\bar{\phi}\right\rangle + \left\langle j\right|\hat{W}\left|\bar{\phi}\right\rangle\right] \\ &= \sum_{j=0}^{\infty}\left\langle j\right|T\left|\bar{\phi}\right\rangle\left|j\right\rangle + \sum_{j,l=0}^{\infty}\left\langle j\right|\hat{W}\left|l\right\rangle\left|\bar{\phi}\right\rangle\left|j\right\rangle]\end{aligned}$$

If we equate the coefficients for each $\left|j\right\rangle$, we arrive at a discrete Schrödinger equation

$$T_jc_j + \sum_{l\neq j}W_{jl}c_l = \epsilon c_j, \tag{3.37}$$

where $\epsilon = -W_{jj}$ and

$$\begin{aligned}&c_j = \langle j|\bar{\phi}\rangle, \\ &T_j = \tan[((j+1/2)\alpha - \Lambda)/2], \\ &W_{jl} = \left\langle j\right|\hat{W}\left|l\right\rangle.\end{aligned} \tag{3.38}$$

The properties of the system (3.37) and the sequence T_j are studied numerically in [27]. In the discussion below, we quote the results of that paper.

For rational q the eigenphases of the Floquet operator are rational fractions of 2π, the eigenstates are delocalized *Bloch waves*, which are wave function solutions $|\phi\rangle$ with the form

$$|\phi(\mathbf{r})\rangle = e^{\mathbf{r}\cdot\mathbf{k}}u(\mathbf{r}),$$

where $\mathbf{r}$ is position, $\mathbf{k}$ is a real vector and u is a periodic function [37]. Bloch waves commonly arise as solutions to problems in crystals, like the problem of an electron on a lattice studied by Anderson. This underlying relationship of the kicked oscillator to the problem of electrons in a crystal is linked to the appearance of the crystal and quasicrystal symmetry observed in the classical system for rational q (see the left panel of Fig. 2.1).

These Bloch wave solutions are unbounded in space (and hence delocalized) and in energy. They have a continuous spectrum and the total energy of the system (3.37) rises as a roughly quadratic function of time. These cases are sometimes called *quantum resonances* in analogy with the classical case, where a rational value of q in $\alpha = 2\pi/q$ is the resonance condition [19].

For irrational q, there is strong numerical evidence (presented in [27]) to suggest that the sequence T_j is a pseudorandom number generator, with the values being distributed roughly according to the Cauchy distribution [36]. In this case, the conclusions of Anderson's study hold and there are localized Floquet eigenstates with a discrete spectrum, the phenomenon dubbed *Anderson localization*. The term *pseudorandom* refers to the fact that the sequence T_j passes computational tests to determine randomness but is not actually random, as we know it to be generated by a deterministic process.

One can study localisation numerically using the *inverse participation ratio* (IPR). Consider a quantum system described by an N-dimensional Hilbert space with basis $\{|j\rangle\}_{j=1,\cdots,N}$ that is in state $|\psi\rangle$. The Born rule guarantees that $p_j = |\langle\psi|j\rangle|^2$ is the probability of finding the system in state $|j\rangle$ upon measurement. For the kicked oscillator we will take $|j\rangle$ to be the number basis. The IPR is [28]

$$\mathrm{IPR} = \frac{1}{\sum_{j=1}^{N} p_j}. \tag{3.39}$$

The IPR can take values between 1 (if the system is in the basis state $|j\rangle$ for some j) and N (if it can be in each basis state $|j\rangle$ uniformly with probability $1/N$). If the IPR is small relative to N, we interpret the system as being localised, as few of the available basis states are occupied.

In Fig. 3.7, we plot the IPR for the kicked oscillator with the cosine potential (3.7) for $K = 2$ and for both rational and irrational q in a system with 2^8 states. In both cases the IPR remains below 60, which is much less than the available 2^8 states. Figure 3.7 only includes the results for the first 100 kicks for clarity, but we have plotted the IPR for up to 100000 kicks and it does not exceed 60 in that time.

For the sawtooth potential with irrational q, the quantum distribution becomes localized very quickly, and this causes the classical and quantum distributions to drift further apart as time goes on. We can see this in the plots of the IPR in Fig. (3.8).

It is worth noting here that for general potentials V, Eq. (3.37) does not describe a true tight-binding model. In order for the comparison to be exact, we need

$$V(\hat{x}) = -2\arctan(k\cos(\hat{x}) - \epsilon). \tag{3.40}$$

See the discussion in [27] for more details on why this is the case. If we plot the potential functions, we see that the sawtooth potential is much closer to the form of (3.40) than the cosine potential, which may account for the more pronounced localization we see in Fig. (3.8b).

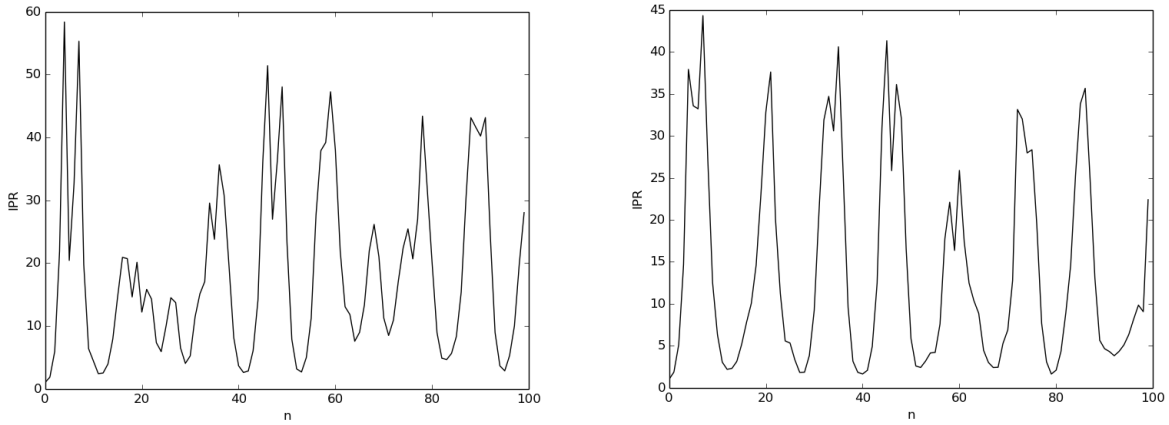

(a) $q = 6$. (b) $q = \sqrt{2}$.

Figure 3.7: IPR (3.39) for the cosine potential with $K = 2$, $\eta = 0.1$ and two values of q. We use a Hilbert Space of dimension 2^8 for the computation. Observe that for both rational and irrational q, the IPR remains small relative to the dimension of the Hilbert Space, suggesting that the quantum distribution spreads over only a small portion of phase space.

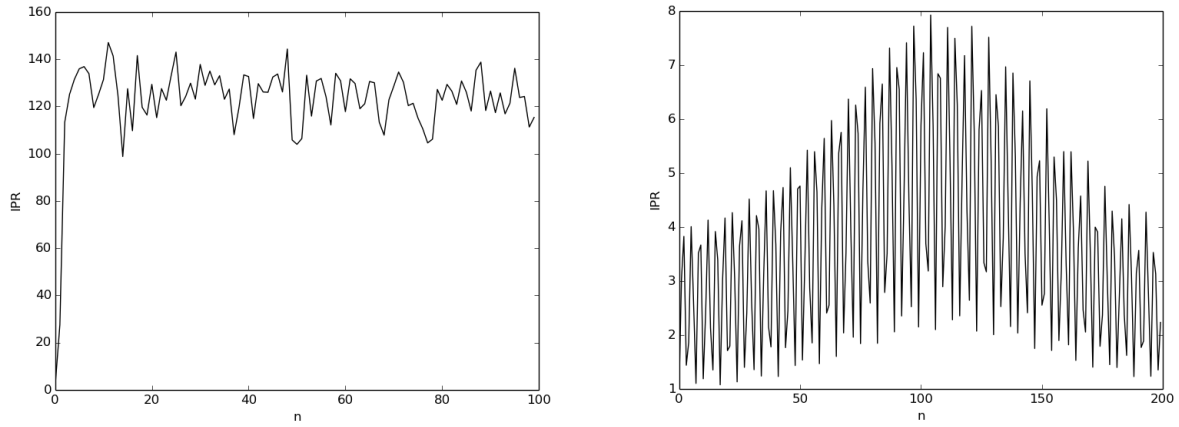

(a) $q = 6$ (b) $q = \sqrt{2}$

Figure 3.8: IPR for the kicked-oscillator sawtooth potential with $L = 6$, $\sigma = 0.1$, and different values of q. We observe Anderson localization for irrational q, and it is far more pronounced than it is for the cosine potential (see Fig. 3.7), with the distribution spreading over only a very small number of the 2^8 possible states. For rational q, we see that after one kick there is a large increase in the IPR, suggesting the that quantum distribution occupies many states. The classical distribution does not spread as rapidly, so this may contribute to the poor quantum–classical correspondence that we have observed for the sawtooth potential.

4 A Dissipative Environment in the Quantum Regime

4.1 Representing the Environment

To represent an open quantum system, we move away from state vectors and into the formalism of *density operators*, which provides a more general setting that allows us to discuss both so-called *pure states* and also statistical mixtures of states. For a quantum system described by a Hilbert Space $\mathcal{H}$ and in a state $|\psi\rangle \in \mathcal{H}$, we define the density operator to be $\hat{\rho} = |\psi\rangle \langle\psi|$, a bounded operator on $\mathcal{H}$. In general, a density operator $\hat{\rho}$ is any bounded operator on $\mathcal{H}$ that is positive, has trace 1, and is self-adjoint.

In this formalism, the Schrödinger equation is replaced by the von Neumann equation [8]:

$$\frac{\partial \hat{\rho}}{\partial t} = -\frac{i}{\hbar}[\hat{H}, \hat{\rho}], \tag{4.1}$$

where $\hat{\rho}$ is the density operator for the system, taken in the Schrödinger picture. Note that although this looks very similar to the Heisenberg equation of motion for an operator in the Heisenberg picture, Eq. (4.1) only makes sense when we take the density operator in the Schrödinger picture (in the Heisenberg picture these operators are constant).

This describes the unitary dynamics of the system, and we introduce the nonunitary effect of the environment by adding the Lindblad operator [42]:

$$\mathcal{L}\hat{\rho} = \sum_i \frac{\gamma_i}{2}(2\hat{c}_i\hat{\rho}\hat{c}_i^\dagger - \hat{c}_i^\dagger\hat{c}_i\hat{\rho} - \hat{\rho}\hat{c}_i^\dagger\hat{c}_i), \tag{4.2}$$

where the collapse operators $\hat{c}_i$ determine the form of the system–environment coupling and the constants γ_i determine the strength of the coupling. Eq. (4.1) is very general and can be derived under the assumption of complete positivity of the density operator, as well as the Markovicity of the system. A quantum system is *Markov* if there is a continual, one-way loss of information to the environment [9]. Although many real environments retain information and may feed it back into the system, resulting in a non-Markovian evolution, Markvoicity is a good approximation provided the memory of the environment is very short. See [42] for a full derivation of Eq. (4.2) and discussion of the assumptions required.

Combining Eq. (4.1) and Eq. (4.2) gives the Lindblad master equation, which describes the influence of the environment on our system:

$$\frac{\partial \hat{\rho}}{\partial t} = -\frac{i}{\hbar}[\hat{H}, \hat{\rho}] + \mathcal{L}\hat{\rho}. \tag{4.3}$$

All that remains is to define the appropriate $\hat{c}_i$ and γ_i for our environment.

We consider dissipation caused by a zero-temperature reservoir with coupling strength Γ, in the case of the weak-coupling limit $\Gamma \ll \omega$. Recall that ω is the frequency of the harmonic oscillator. This weak-coupling assumption implies that the system undergoes many oscillations within the decay time, allowing us to use the rotating-wave approximation, where one neglects rapidly-oscillating terms in a Hamiltonian [56]. In this case the coupling can be described by a single operator $\hat{a}$, the harmonic oscillator annihilation operator [12]. If we define $\hat{H}'$ to be a

Hamiltonian with the same form as in Eq. (3.1) but with ω replaced by the Ω from Eq. (2.11), as in the classical case, then Eq. (4.3) becomes:

$$\frac{\partial\hat{\rho}}{\partial t} = -\frac{i}{\hbar}[\hat{H}', \hat{\rho}] + \frac{\Gamma}{2}(2\hat{a}\hat{\rho}\hat{a}^\dagger - \hat{a}^\dagger\hat{a}\hat{\rho} - \hat{\rho}\hat{a}^\dagger\hat{a}). \tag{4.4}$$

The choice of frequency Ω ensures that the classical and quantum frequencies coincide. As with our choice of model for the classical system, there are many other ways that we could introduce dissipation (including some in which we would not need the weak-coupling assumption) but this is the simplest. Another common choice is the Caldeira–Legget model [10].

It is important to note that Eq. (4.4) is not completely equivalent to the classical system described in Chapter 2.3. The two situations are difficult to reconcile: a classical distribution subject only to dissipation collapses to a point distribution (i.e., a probability distribution with all of the weight on one point), whereas a quantum distribution ends up in a ground state, which must have some finite width due to the uncertainty principle. Our results will be valid in the semiclassical limit, but will not correspond directly to the fully classical case based on the map (2.10) [12]. We expect the uncertainty principle to play an important role in the dynamics around the system's fixed points. We will return to this idea in Chapters 4.3 and 4.4.

It is also worth making a few remarks about the subject of non-Markovian environments. These can be described by an equation of the same form as Eq. (4.3) but now the Hamiltonian, the collapse operators, and the coupling strengths can depend on time (even if the Hamiltonian is time-independent before the introduction of an environment).

A time-dependent version of the Lindblad operator always generates completely positive dynamics provided the $\gamma_i(t)$ are non-negative for all times. This is the Gorini–Kossakowski–Sudarshan–Lindblad theorem [25, 42]. It is an interesting open problem to formulate general necessary and sufficient conditions for a time-dependent Lindblad equation to lead to such dynamics [9]. It would be informative to study a system like the delta-kicked oscillator in the presence of such a non-Markovian environment, although that is beyond the scope of this dissertation.

4.2 Evolution Operator

The addition of the extra terms to the von Neumann equation requires us to revisit the evolution operator. If we turn off the delta-kick, we can rewrite Eq. (4.4) as

$$\frac{\partial\hat{\rho}}{\partial t} = \hat{S}\hat{\rho} \tag{4.5}$$

which uses a *superoperator* $\hat{S}$ defined by

$$\hat{S}\hat{\rho} = -\frac{i}{\hbar}[\hat{H}_0, \hat{\rho}] + \frac{\Gamma}{2}\left(\left[\hat{a}\hat{\rho}, \hat{a}^\dagger\right] + \left[\hat{a}, \hat{\rho}\hat{a}^\dagger\right]\right),$$

where $\hat{H}_0$ is the harmonic-oscillator Hamiltonian with frequency Ω. A superoperator is a linear operator that acts on a vector space of linear operators. In the context of quantum mechanics, the term refers more specially to a completely positive map that preserves the trace of its argument, which is necessary to ensure that it does not generate density operators that violate the uncertainty principle. Any master equation of the form (4.3) can be written in the form of Eq. (4.5) with the definition of an appropriate superoperator [4].

Formally, the evolution of the density operator is then given by

$$\hat{\rho}(t) = \exp(\hat{S}t)\hat{\rho}(0).$$

Finally, we turn the delta-kick back on by adding $\hat{F}_{\text{kick}}$, the part of the Floquet operator (3.2) associated with the delta-kick, to obtain an equation for the density operator just before the $(n+1)$st kick:

$$\hat{\rho}_{n+1} = \exp(\hat{S}\tau)\hat{F}_{\text{kick}}\hat{\rho}_n\hat{F}^{\dagger}_{\text{kick}}. \tag{4.6}$$

4.3 Cosine Potential

The result of adding a dissipative environment to kicked systems with this sort of potential has been well-studied in the literature [34] and covered in textbooks such as [29]. Prior research has determined that quantum interference effects are extremely sensitive to perturbations produced by an environmental reservoir. This implies that the quantum and classical distributions should remain closer together than they did in the closed system. Results for the breaking time have been determined by several methods, and these do indeed predict better quantum–classical correspondence than we had for the closed system [12, 34].

In Fig. 4.1, we see that the quantum dissipative kicked oscillator with the cosine potential is (at least visually) very close to its classical analague, though small-scale structures in phase space are not present, as is evident from comparing with Fig. 2.8. Importantly, the quantum distribution does lie in the same region of phase space as the classical attractor.

A good correspondence is to be expected, as Fig. 2.9a indicates that the dynamics get closer to being integrable for certain values of $\Gamma\tau/2$, and our choice of 0.36 for this parameter lies close to the region of integrability near $\Gamma\tau/2 = 0.4$.

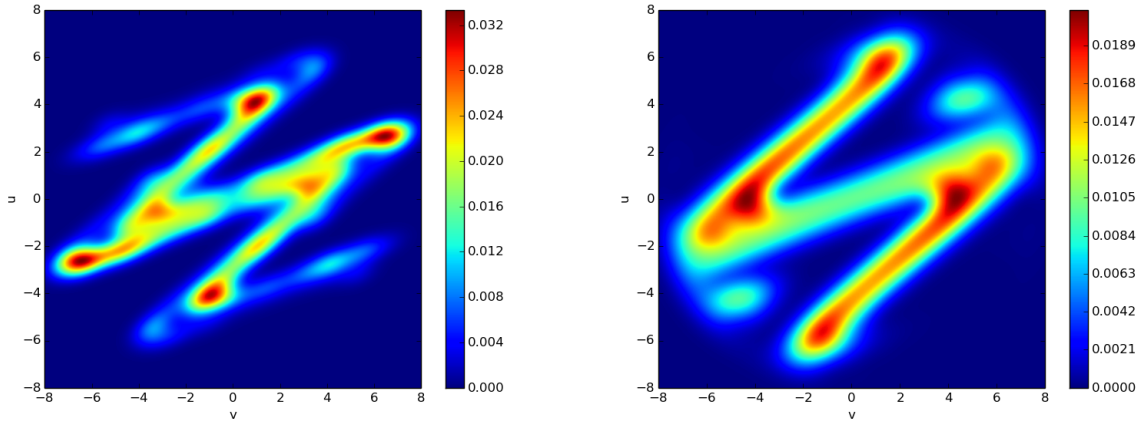

Figure 4.1: (Left) Classical PDF for the dissipative kicked oscillator with the cosine potential after 9 kicks for $\bar{K} = 6$, $q = 6$, and $\Gamma\tau/2 = 0.36$. (Right) Wigner function for the analagous quantum system using the same parameter values and $\eta = 0.5$. Although there is a good correspondence between the two plots, small-scale structures from the classical system are not present in the quantum system. It looks like the Wigner function does have any negative regions, seemingly a contradiction of the known fact that it must take negative values somewhere. This is because the regions of negative probability are smaller than the size of the cells in the grid over which we compute the function. The fact that these regions are so small predicts that we obtain a better quantum–classical correspondence than in the system without a reservoir, where visible quantum interference patterns appeared in a Wigner function computed on a grid of the same size ($10^3 \times 10^3$).

For the dissipative kicked oscillator with the cosine potential, the characteristic function is almost the same as that given by Eq. (3.11). The only difference is that the first term in (3.12) is now

$$\lambda_k = \lambda_{k-1} e^{i\bar{\alpha}} e^{-\Gamma\tau/2} + i m_k \eta, \tag{4.7}$$

where Γ is the coupling strength introduced in Chapter 2.3. In addition to the harmonic rotations caused by the first exponential term, exponential decay results from dissipative drift [12].

The breaking time now also depends on the values of this dissipation strength Γ. One can calculate the breaking time by the same approach as in the case without a reservoir. We summarise the results for the $|\bar{K}\sin(\alpha)| \gg 1$ case in Table 1:

Nonlinearity Strength	$\Gamma\tau/2 < \ln(\eta/2)$	$\Gamma\tau/2 > \ln(\eta/2)$
$\ln(\bar{K}\sin(\bar{\alpha})) > \Gamma\tau/2$	(a) $t_\hbar \approx 1$ kick	(c) $t_\hbar \approx \frac{\ln(2\bar{K}/\eta)}{\ln(\bar{K}\sin(\bar{\alpha}))-\Gamma\tau/2}$
$\ln(\bar{K}\sin(\bar{\alpha})) < \Gamma\tau/2$	(b) $t_\hbar \approx 1$ kick	(d) $t_\hbar \to \infty$

Table 1: The breaking times for the dissipative kicked oscillator with the cosine potential in various parameter regions.

The first column in Table 1 corresponds to a *deep quantum regime* [12] characterised by

$\Gamma\tau/2 < \ln(\eta/2)$, where a single kick is enough to separate the quantum and classical predictions, regardless of the strength of the nonlinearity. It is interesting that even when the value of Γ is large enough so that the classical system is in a non-chaotic regime, the correspondence is still lost.

In the *weak quantum regime* for which $\Gamma\tau/2 > \ln(\bar{K}\sin(\bar{\alpha}))$, the nonlinearity strength becomes important. For case (d), the dissipation is strong enough to suppress the classical chaos; Fig. 2.9a shows that for these values of $\Gamma\tau/2$, the LEs are all negative and the dynamics are non-chaotic, so we would expect the Ehrenfest theorem to be obeyed in this parameter region.

Case (c) is more interesting. The expression for $t_\hbar$ in (c) is very similar to that given by Eq. (3.14), with the addition of the term dependent on the dissipation strength in the denominator. One can increase this value by decreasing the value of $\Gamma\tau/2$, although this hides the fact that for certain values of $\Gamma\tau/2$ below the critical value at which the origin becomes stable (approximately 0.51 in the case $\bar{K} = 6$, $q = 6$) the classical system is not chaotic, as we can see in Fig. 2.9a. If we wish to maintain the presence of a chaotic attractor in the classical phase space, it is not possible to make the breaking time arbitrarily large and there is a some point at which quantum and classical predictions diverge from one another [34].

We can compare the breaking time (c) with that for the system without a reservoir, given by Eq. (3.14). The ratio between the breaking times is

$$\frac{\tau_\hbar^{\text{dis}}}{\tau_\hbar} = \frac{\ln(\bar{K}\sin(\bar{\alpha}))}{\ln(\bar{K}\sin(\bar{\alpha})) - \Gamma\tau/2}. \tag{4.8}$$

The maximum increase in breaking time occurs when $\Gamma\tau/2$ is large enough relative to $\bar{K}$ to make all the LEs negative. For $\bar{K} = 6$, this gives an increase in breaking time by a factor of about 1.5. Even for large $\bar{K}$, numerical simulations illustrate that this increase is small: for $\bar{K} = 500$, the increase is less than a factor of 4.

In Fig. 4.2, we compare the variance in position ($\Delta^2 v$) of the distributions for both the classical and quantum systems. The classical and quantum distributions both exhibit similar asymptotic behaviour even though they differ in the measure in Eq. (3.16). They also have roughly the same stationary behaviour as the number of kicks n becomes large. However, as we noted in Chapter 3.4 this behaviour of the second moment does not imply that the complete phase space distributions follow the same pattern, as we can see from the Wigner function in Fig. 4.1.

Overall, dissipation does seem to bring the classical and quantum systems into much better correspondence even though it does not necessarily result in a large increase in breaking time. It does break down small-scale structures in phase space, leading to distributions that are visually similar (see Fig. 4.1), and induces regions of parameter values for which the kicked oscillator is non-chaotic, resulting in an infinite breaking time (i.e., (d) in Table 1).

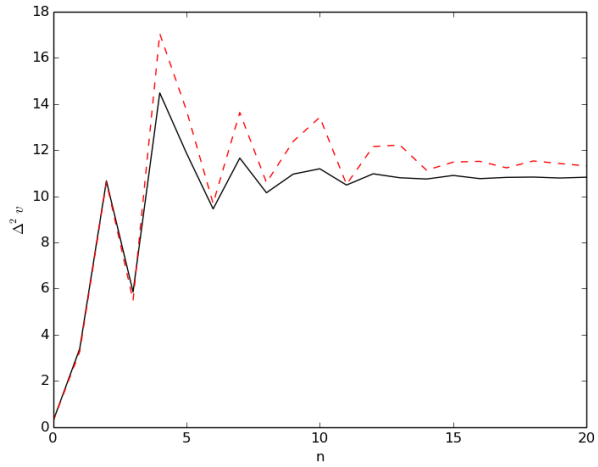

Figure 4.2: Plots of $\Delta^2 v$ for the classical (red dashed curve) and quantum (black solid curve) distributions for $\bar{K} = 6$, $\Gamma\tau/2 = 0.36$, $q = 6$, and $\eta = 0.5$. Even after the breaking time ($t_\hbar \approx 4$ kicks), the systems still follow similar asymptotic behaviour.

As before, we can consider the case $|\bar{K}\sin(\alpha))| \ll 1$. In the deep quantum regime (i.e., $\Gamma\tau/2 < \ln(\eta/2)$) we still have $t_\hbar \approx 1$ kick. For the breaking time in the weak quantum regime (i.e., $\Gamma\tau/2 > \ln(\eta/2)$), we obtain the result

$$t_\hbar \approx \frac{e^{\Gamma\tau}}{K\eta^2}. \tag{4.9}$$

We derive Eq. (4.9) in the same manner as Eq. (3.15), except that we now also have the dissipative drift term.

We saw in Chapter 2.3, for small values of $\bar{K}$, the kicked-oscillator system with the cosine potential has no positive LEs for any value of Γ, suggesting the system is non-chaotic. Because of this, we might expect better correspondence in this regime than Eq. (4.9) suggests.

The reason for the lack of correspondence between the classical and quantum distributions is due to the fact that, as we remarked in Chapter 4.1, the two systems are not entirely the same. The classical system collapses to a point distribution at the origin, as we expect, and we can see from Fig. (4.3) that the quantum system converges to a coherent state centred at the origin. From numerical experiments, the variances of the distribution after 9 kicks are $(\Delta^2 v, \Delta^2 u) \approx (1.194, 0.912)$. Because $\eta = 0.5$ and these operators obey the uncertainty relation $(\Delta^2 v)(\Delta^2 u) \geq 2\eta$, we see this is close to a minimum-uncertainty state. It becomes one in the limit $n \to \infty$.

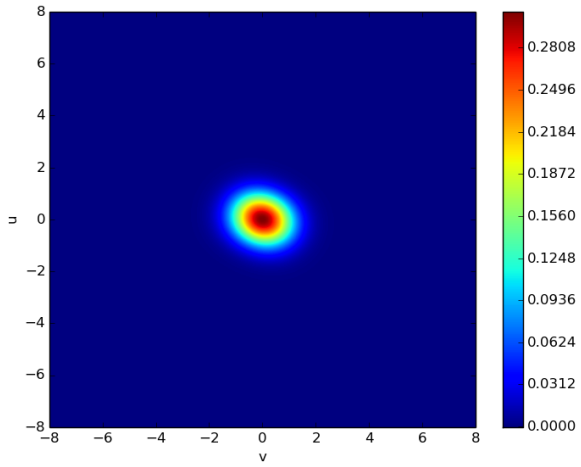

Figure 4.3: Wigner distribution for the dissipative kicked oscillator with the cosine potential for $\bar{K} = 0.5$, $q = 6$ and $\eta = 0.5$ after 9 kicks. This is almost a minimum-uncertainty state centred at the origin, as suggested by computing the variances in position and momentum, which give $(\Delta^2 v)(\Delta^2 u) \approx 2\eta$.

4.4 Sawtooth Potential

We now return to the sawtooth potential (1.5), for which we observed a very poor correspondence between the quantum and classical systems at all times in the closed system. In Fig. 4.4, we show a comparsion between the classical PDF and the quantum Wigner function for the dissipative kicked-oscillator with the sawtooth potential. Clearly, there is a better correspondence than we observed for the closed system in Fig. (3.5), but this correspondence is still not as good as it is for the dissipative kicked oscillator with the cosine potential (see Fig. 4.1). While the Wigner function for the cosine potential lies entirely in the same region as the classical attractor shown in Fig. 2.8, the Wigner function does not when we use a sawtooth potential. It does have the 'bars' of positive probability in roughly the correct region.

As with the cosine potential, stronger dissipation produces a better correspondence between the quantum and classical distributions because the dynamics become completely dominated by the environment for $\Gamma \gg 1$.

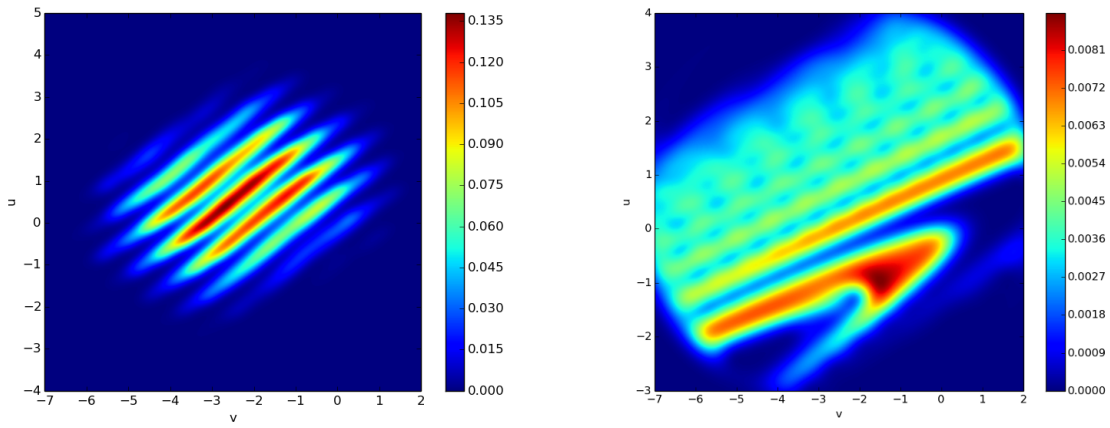

Figure 4.4: (Left) Classical PDF for the dissipative kicked oscillator with the sawtooth potential after 10 kicks, for $\bar{L} = 6$, $q = 6$, and $\Gamma\tau/2 = 0.36$. (Right) Wigner function for the quantum system using the same parameter values and $\sigma = 0.1$. We observe a much better correspondence in the open system than for the closed system in Fig. 3.5, however visually we still observe many differences between the distributions. As with the cosine potential, note the lack of regions of negative probability, which occurs because the dissipation makes the quantum interference fringes smaller than the grid over which we plot the Wigner function.

The characteristic function is identical to that given by Eq. (3.25), except with a change to the first term in Eq. (3.24):

$$\lambda_k = \lambda_{k-1} e^{i\bar{\alpha}} e^{-\Gamma\tau/2} + i s_k \xi_k \sigma. \tag{4.10}$$

We repeat the calculations of Chapter 3.5 to estimate the values of $|s_k|$, and we obtain

$$\begin{aligned} |s_1| &\sim \frac{\bar{L}}{\sigma\xi_1} e^{-\Gamma\tau/2} \left| \lambda e^{i\bar{\alpha}} + \lambda^* e^{-i\bar{\alpha}} \right|, \\ &\vdots \\ |s_n| &\sim \frac{\bar{L}}{\sigma\xi_n} \left| (\lambda e^{ni\bar{\alpha}} + \lambda^* e^{-ni\bar{\alpha}}) e^{-n\Gamma\tau/2} - 2\xi_1 s_1 \sigma \sin((n-1)\bar{\alpha}) e^{-(n-1)\Gamma\tau/2} - 2\xi_{n-1} s_{n-1} \sigma \sin(\bar{\alpha}) e^{-\Gamma\tau/2} \right|. \end{aligned} \tag{4.11}$$

For $|\bar{L}\sin(\bar{\alpha})| \gg 1$, we have

$$\begin{aligned} |s_1| &\sim \frac{\bar{L}\sin(\bar{\alpha})}{\sigma\xi_1} e^{-\Gamma\tau/2}, \\ &\vdots \\ |s_{Mn}| &\sim \frac{(\bar{L}\sin(\bar{\alpha}))^{Mn}}{\sigma\xi_n} e^{-Mn\Gamma\tau/2}. \end{aligned} \tag{4.12}$$

We now examine when $|\mu_k| \ll 1$ holds. The ratio between two consecutive values of μ is

$$\begin{aligned} \frac{|\mu_k|}{|\mu_{k-1}|} &\approx \bar{L}\sin(\bar{\alpha})\left(1-\frac{1}{\xi_k}\right)e^{-\Gamma\tau/2}, \qquad k \in 1,\ldots,Mn, \\ |\mu_1| &\approx \frac{\sigma e^{-\Gamma\tau/2}}{2}. \end{aligned} \tag{4.13}$$

If $\Gamma\tau/2 < \ln(2/\sigma)$, then $|\mu_1| > 1$, and the correspondence between the quantum and classical characteristic functions is lost after the first kick. The occurs when $\Gamma\tau/2 < \ln(\sigma/2)$. Again, we call this region the deep quantum regime, and $t_\hbar \approx 1$ kick in this case.

If $\Gamma\tau/2 > \ln(\sigma/2)$ (i.e., the weak quantum regime), two possibilites can occur. If $|\mu_k|/|\mu_{k-1}| < 1$, the μ_k decrease with increasing of k. Because $\mu_1 < 1$, each term is smaller than 1. This means the quantum characteristic function (3.25) is always a good approximation of the classical one[1], and quantum–classical correspondence is good at all times. This occurs when

$$\frac{\Gamma\tau}{2} > \ln\left[\left(1-\frac{1}{M}\right)\bar{L}\sin(\bar{\alpha})\right], \tag{4.14}$$

as $\xi_k \leq M$ for all k. In the limit $M \to \infty$, the condition (4.14) reduces to $\Gamma\tau/2 > \ln(\bar{L}\sin(\bar{\alpha}))$, and the breaking time $t_\hbar \to \infty$.

Finally, when $\Gamma\tau/2 < \ln(\bar{L})$ the sequence $\{\mu_k\}$ increases, and we should expect there to be some k for which $\mu_k \approx 1$. As before, for large M this occurs after just one kick, as $\mu_M \to \infty$.

So for the sawtooth potential (1.5), there are only two cases: (1) In the weak quantum regime (i.e., $\Gamma\tau/2 > \ln(\sigma/2)$) with $\Gamma\tau/2 > \ln(\bar{L}\sin(\bar{\alpha}))$, then $t_\hbar \to \infty$; (2) otherwise $t_\hbar \approx 1$ kick. This contrasts with the cosine potential, where there exists a parameter regime that gives us a finite expression for the breaking time that is larger than 1 kick ((c) in Table 1).

In Fig. 4.5, we show that, as with the cosine potential, the variances in the distributions differ transiently but exhibit similar scaling behaviour. The distributions remain some distance apart (with respect to the distance (3.16)) at all times, which is borne out both by our analysis and Fig. 4.4, which suggests that the distributions, while similar, still have many different features, as we can see in Fig. 4.4.

[1]Recall from Chapter 3.5 that the arguments of the Bessel functions in the quantum and classical characteristic equations (3.25) and (3.26) are approximately the same when $\mu_1 \ll 1$

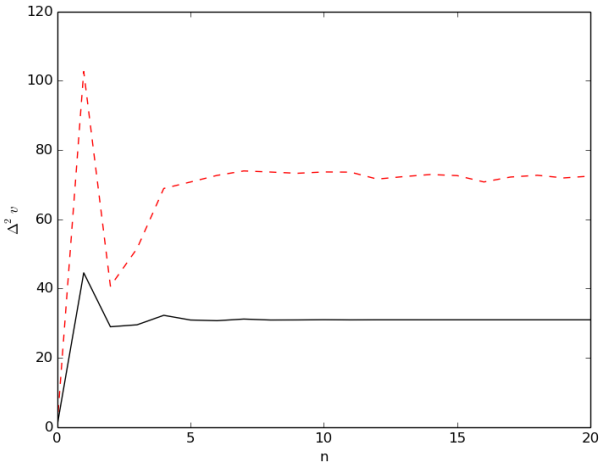

Figure 4.5: Variance in position for the classical (red dashed curve) and quantum (black solid curve) distributions of the dissipative kicked oscillator with the sawtooth potential and parameter values $\bar{L} = 6$, $\Gamma\tau/2 = 0.36$, $q = 6$, and $\sigma = 0.5$. Unlike for the cosine potential, the distributions remain apart at all times, although they exhibit similar asymptotic behaviour.

Once again, we consider the case of $\bar{L} \ll 1$ and $\sin(\bar{\alpha}) \approx 1$. We obtain

$$\begin{aligned}
|s_1| &\approx \frac{\bar{L}e^{-\Gamma\tau/2}}{\sigma\xi_1}, \\
|s_2| &\approx \frac{\bar{L}^2e^{-\Gamma\tau}}{\sigma\xi_2}, \\
|s_3| &\approx \frac{\bar{L}e^{-\Gamma\tau/2}}{\sigma\xi_1} + \frac{L^3e^{-3\Gamma\tau/2}}{\sigma\xi_3}, \\
&\vdots \\
|s_{2n-1}| &\approx \frac{\bar{L}e^{-\Gamma\tau/2}}{\sigma\xi_1} + (2n-3)\frac{\bar{L}^3e^{-3\Gamma\tau/2}}{\sigma\xi_3} + O(\bar{L}^5), \\
|s_{2n}| &\approx \frac{n\bar{L}^2e^{-\Gamma\tau}}{\sigma\xi_2} + O(\bar{L}^4),
\end{aligned} \tag{4.15}$$

which implies that

$$|\mu_k| \approx \begin{cases} m\bar{L}^2\sigma\xi_3 e^{-3\Gamma\tau/2}, & k = 2m-1, \\ m\bar{L}\sigma\xi_2 e^{-\Gamma\tau}/2, & k = 2m, \end{cases} \tag{4.16}$$

with ξ_k as in (3.24) and $|\mu_1|$ given by Eq. (4.13) as before. In the deep quantum regime described above, $t_\hbar \approx 1$ kick as $|\mu_1| > 1$. In the weak quantum regime, we consider the ratio between consecutive μ and find that

$$\frac{|\mu_k|}{|\mu_{k-1}|} \approx \begin{cases} 3\bar{L}e^{-\Gamma\tau/2}, & k = 2m-1, \\ e^{\Gamma\tau/2}/(3\bar{L}), & k = 2m. \end{cases} \tag{4.17}$$

Clearly, no bound on $\Gamma\tau/2$ can ensure that that both cases of (4.17) remain less than 1, so we no longer have separate cases based on this value as we did above for $|\bar{L}\sin(\bar{\alpha})|\gg 1$. Instead, we obtain a breaking time of

$$t_\hbar \approx \frac{e^{\Gamma\tau}}{\bar{L}\sigma}. \tag{4.18}$$

For $\bar{L} < 1$ and any $\Gamma > 0$, our numerical calculations show that the system has no positive LE, so we expect a good correspondence as Γ grows large. We observe that by increasing the value of Γ while holding σ fixed in Eq. (4.18), we can make the breaking time arbitraily large. This is expected, as for sufficently large Γ the classical dynamics given by Eq. (2.9) are dominated by the environment.

As with the cosine potential, while the classical distribution collapses to a single point after enough time has passed – numerical results show this point is about $(v, u) = (-0.279, 0.063)$ for the sawtooth potential – this is impossible for the quantum system. In Fig. 4.6, we show the Wigner function for $\bar{L} = 0.5$, the corresponding variance in position, and the variance in position for the associated classical system with the same parameters. We see that although the classical variance approaches 0, as we expect, the variance in the quantum distribution does not settle down to a constant value. This illustrates an important difference between the kicked oscillator with the cosine and sawtooth potentials, as the latter converges to a coherent state at the origin.

The 'spikes' seen in Fig. 4.6 are possibly evidence of *Bloch Oscillations*. These oscillations have been observed in quantum chaotic systems [46] and in Bose–Einstein Condensates [38]. They often occur in problems related to lattices, and we have shown the kicked oscillator with the sawtooth potential is closely related to such a problem (see Chapter 3.6). We have been unable to prove these 'spikes' represent Bloch oscillations, and this would be an interesting area for further research.

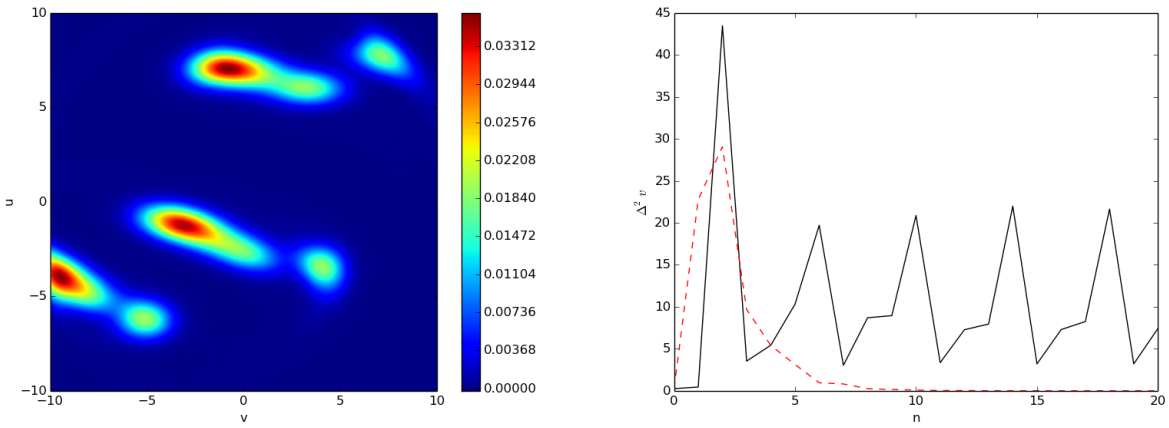

Figure 4.6: (Left) Plot of the Wigner function for the dissipative kicked oscillator with the sawtooth potential and parameter values $\bar{L} = 0.5$, $q = 6$, and $\sigma = 0.1$. The distribution is clearly not a minimum-uncertainty state. (Right) Variances in position for the classical (red dashed curve) and quantum (black solid curve) distributions with the same parameters. This confirms that the classical distribution collapses to a point, however the quantum distribution does not converge to a minimum-uncertainty state. Numerical calculations of the variance in momentum include spikes at the same values of n as with the variance in position. Note the pattern of the spikes repeats after about $n = 7$.

4.5 Localization

In Chapter 3.6 we discussed the eigenstates $|\phi\rangle$ of the Floquet operator (3.2)

$$\hat{F}\,|\phi\rangle = e^{-i\Lambda}\,|\phi\rangle\,.$$

In the conservative case, these form a natural basis, which is not true in the dissipative system because the environment induces incoherent transitions between Floquet states, causing them to decay exponentially [14]. However, in a similar vein to the preservation of invariant tori under small perturbations, for sufficently weak dissipation these transitions act as a perturbation on the conservative system, and the Floquet eigenstates still provide a good basis for a description of the dynamics (at least on sufficiently short time scales).

Our analysis of localization in the kicked oscillator in Chapter 3.6 still holds when the coupling strength $\Gamma \ll 1$. As Γ increases, our analysis is no longer valid. Figures 4.7 and 4.8 no not show localization in the dissipative kicked oscillator even for irrational q, which helps to promote better correspondence between the systems even on time scales that exceed the breaking time.

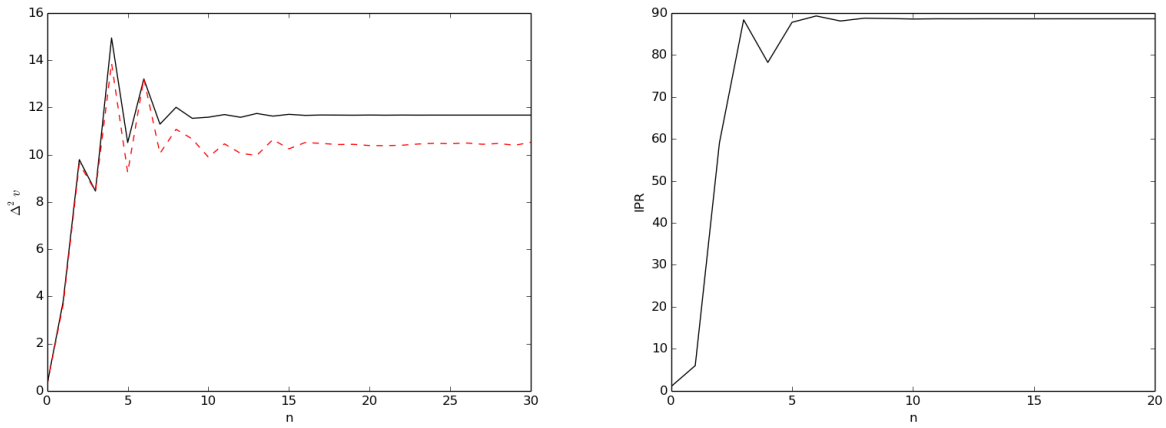

Figure 4.7: (Left) Variances in the distribution for both the classical (red dashed curve) and quantum (black solid curve) dissipative kicked-oscillator systems with the cosine potential for parameter values $\bar{K} = 6$, $\Gamma\tau/2 = 0.36$, $\eta = 0.5$, and $q = \sqrt{2}$. Up to the breaking time (at $t_\hbar \approx 7$ kicks), the distributions remain close together, as for the choice of $q = 6$. After the breaking time, they drift apart but exhibit similar asymptotic behaviour. There is no sign of Anderson localization that we observed for irrational q in the system without a reservoir. To arrive at the Anderson model in Eq. (3.37), we exploited the underlying lattice structure of the kicked oscillator, and the absence of Anderson localization here suggests that dissipation has destroyed this structure. (Right) IPR (see Eq. (3.39)) as the number of kicks increases. The system eventually settles down to a constant value near 90. This is to be expected, as the classical distribution remains bounded in space (see Fig. (2.8)).

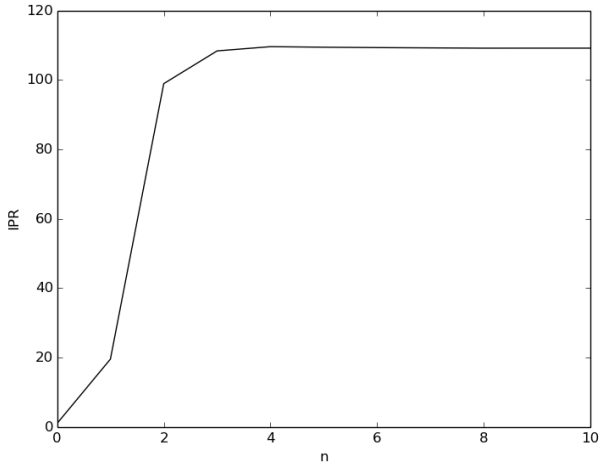

Figure 4.8: IPR for the dissipative kicked oscillator with the sawtooth potential and $\bar{L} = 6$, $q = 6$ and $\sigma = 0.1$. The number of states in the Hilbert Space is 2^8. The IPR increases rapdily with the number of kicks before settling at about 110.

5 Conclusions

In this thesis, we presented a treatment of the quantum–classical transition in the delta-kicked oscillator with two different potentials, the cosine potential (1.4) and the sawtooth potential (1.5). We studied the kicked oscillator because it is a simple model that is mathematically tractable, while also exhibiting behaviours such as localization and a finite breaking time that occur in a variety of quantum chaotic systems. We also studied the kicked oscillator in the presence of a dissipative environment, which helps one to understand how such environments can affect the dynamics of quantum chaotic systems. This is important for experiments on quantum chaos, for which we often cannot fully remove environmental effects. It is important to know what impact they have on our experiment's results.

For both the cosine and sawtooth potentials, we obtained expressions for the breaking time for both large and small values of the kick strength. Our results agree with the asymptotic estimate given in [6]. We also performed numerical experiments that support our estimates for the breaking time. We paid special attention to the case of a low kick strength, which is not as well studied as the case of high kick strength in the quantum regime. In this regime, the transition from non-chaotic to chaotic behaviour occurs, and studying this change gives insight into how chaos arises in both classical and quantum systems [58]. For example, KAM theory suggests that many of the intergrable tori of the classical system remain, so we would expect the quantum–classical correspondence to last longer. Our analytical and numerical calculations both support this intuition.

Our numerical experiments for the sawtooth potential agree with our estimate of the breaking time being just one kick in the case of a high kick strength, which seems to be due to a rapid increase in the number of states that are occupied (see Fig. (3.8)). The associated classical system does not spread as rapidly in phase space.

We discussed localization in the kicked osciallator with both potentials and presented an argument that the system can be put into the form of a tight-binding model, for which one obtains periodic solutions when the parameter q is rational and Anderson localization when q is irrational. Our numerical calculations of the IPR (3.39) support this argument by showing that the quantum distribution spreads to only a few of the available states for irrational q.

We studied the quantum kicked oscillator in the presence of a dissipative environment created by coupling the system to a single dissipative reservoir. We showed that this environment can extend the time of quantum–classical correspondence by preventing the formation of small structures in phase space [12]. We observed that the environment also reduces the impact of localization, promoting a longer correspondence time even for the sawtooth potential where—despite the breaking time still being just a single kick in most cases—the variances in the distributions still exhibit similar asymptotic behaviour as the number of kicks n goes to infinity.

Our results for the cosine potential are consistent with prior results, while our investigation for the sawtooth potential in the quantum regime is novel. Our study of this more complicated function shows that in a chaotic regime the quantum–classical correspondence can be lost immediately (i.e., the breaking time is 1 kick), even in the closed system. We also observe that in this case dissipation is not enough to restore correspondence, except when it is so strong that the chaotic dynamics are suppressed completely. We also show that the effects of localisation on the system for irrational q are much larger with the sawtooth potential than with the cosine potential, perhaps due to the fact that it closer to being a true tight-binding model.

It should be possible to test our results using physical experiments. The kicked oscillator has been realised experimental by a photon placed in an ion-trap and kept there with laser pulses [24]. This experimental system is well-studied for the cosine potential [7, 15], and although the sawtooth potential is a somewhat more complicated function it should be possible to realise it as well in this kind of experiment. Our model for the environment is also realisable, as it can be produced by a weakly-coupled zero-temperature reservoir [48].

The above possiblities not withstanding, experimental confirmation of our results is difficult because of decoherence and diffusion, which mask both the breaking time and the localization, restoring correspondence [18, 30]. Our study of dissipation in the kicked oscillator illustrates that dissipation can mask the effects of chaos, a phenomenon that occurs in many other quantum chaotic systems [11]. Although we have not studied any kind of diffusive environment, it is known that this can have a larger effect on the suppression chaos than dissipation, and is hard to control completely in an experimental setting [12].

It would be instructive to study the quantum kicked oscillator with the sawtooth potential in the non-chaotic regime in greater depth. Lowenstein presented an exhaustive treatment of different types of dynamics that arise in the associated classical system (e.g., 'sticky orbits' and 'super-diffusion') for certain parameter values [39, 43], and developed techniques for the analysis of similar systems [44]. From a mathematical perspective, it would be instructive to analyse the quantum system in a similar way to determine whether such varied dynamics still arise and to derive quantum analogues for the techniques presented in [44]. Some work has already been done in this area, particularly on quantum mushroom billards, which also have 'stickiness' [3].

It is also be possible to study the behaviour of the kicked oscillator in the presence of other kinds of environments. For example, dissipative, phase and thermal reservoirs have already been produced in ion-trap experiments [41], so these situations are worth studying. As we mentioned at the beginning of Chapter 4, one can also consider a non-Markovian environment.

References

[1] V. I. Arnold. Proof of a theorem of A. N. Kolmogorov on the preservation of conditionally periodic motions under a small perturbation of the Hamiltonian. *Uspehi Mat. Nauk*, 18:13, 1963.

[2] V. I. Arnold, A. Weinstein, and K. Vogtmann. *Mathematical Methods of Classical Mechanics*. Springer, 1978.

[3] A. H. Barnett and T. Betcke. Quantum mushroom billiards. *Chaos*, 17:043125, 2006.

[4] S. M. Barnett and P. M. Radmore. *Methods in Theoretical Quantum Optics*. Clarendon Press, Oxford, 1997.

[5] C. Beck and F. Schlögl. *Thermodynamics of Chaotic Systems: An Introduction*. Cambridge University Press, London, 1993.

[6] G. P. Berman and G. M. Zaslavsky. Condition of stochasticity in quantum nonlinear systems. *Physica A*, 91:450, 1978.

[7] T. P. Billam and S. A. Gardiner. Quantum resonances in an atom-optical delta-kicked harmonic oscillator. *Physical Review A*, 80:023414, 2009.

[8] H. Breuer. *The Theory Of Open Quantum Systems*. Oxford University Press, 2002.

[9] H. Breuer, E. Laine, J. Piilo, and B. Vacchini. Non-Markovian dynamics in open quantum systems. `http://arxiv.org/abs/1505.01385`, 2015.

[10] A. Caldeira and A. J. Leggett. Influence of dissipation on quantum tunneling in macroscopic systems. *Physical Review Letters*, 46:211, 1981.

[11] G. Carlo, G. Benenti, G. Casati, and D. L. Shepelyansky. Quantum ratchets in dissipative chaotic systems. *Physical Review Letters*, 94:164101, 2005.

[12] A. R. R. Carvalho, R. L. de Matos Filho, and L. Davidovich. Environmental effects in the quantum-classical transition for the delta-kicked harmonic oscillator. *Physical Review E*, 70:026211, 2004.

[13] A. A. Chernikov, R. Z. Sagdeev, D. A. Usikov, and G. M. Zaslavsky. Symmetry and chaos. *Computers and Mathematics with Applications*, 17:17, 1989.

[14] B. V. Chirikov and G. Casati. *Quantum Chaos: Between Order and Disorder*. Cambridge University Press, 1995.

[15] J. I. Cirac, P. Zoller, and S. A. Gardiner. Quantum chaos in an ion trap: the delta-kicked harmonic oscillator. *Physical Review Letters*, 79:4790, 1997.

[16] M. V. Daly. Classical and quantum chaos in a non-linearly kicked harmonic oscillator. *PhD Thesis, Dublin City University*, 1994.

[17] R. L. Devaney. *An Introduction to Chaotic Dynamical Systems*. Addison–Welsey, 1989.

[18] T. Dittrich and R. Graham. Continuous quantum measurements and chaos. *Physical Review Letters A*, 42:4647, 1990.

[19] T. Dittrich and R. Graham. Effects of weak dissipation on the long term behaviour in the quantised standard map with dissipation. *Europhysics Letters*, 7:287, 1990.

[20] G. Floquet. Sur les equations differentielles lineaires a coefficients periodiques. *Annales de l'ecole Normale Superieure*, 12:47, 1883.

[21] P. Frederickson, J. Kaplan, E. Yorke, and J. Yorke. The Lyapunov dimension of strange attractors. *Journal of Differential Equations*, 49:185, 1983.

[22] V. Y. Rubaev G. P. Berman and G. M. Zaslavsky. The problem of quantum chaos in a kicked harmonic oscillator. *Nonlinearity*, 42:543, 1991.

[23] C. W. Gardiner. *Quantum Noise*. Springer, 1991.

[24] S. A. Gardiner. Quantum measurement, quantum chaos, and Bose–Einstein condensates. *PhD Thesis, Leopold-Franzens-Universit at Innsbruck*, 2000.

[25] V. Gorini, A. Kossakowski, and E. C. G. Sudarshan. Completely positive dynamical semigroups of n-level systems. *Journal of Mathematics and Physics*, 17:821, 1976.

[26] P. Grassberger and I. Procaccia. Measuring the strangeness of strange attractors. *Physica D*, 9:189, 1983.

[27] D. R. Grempel, S. Fishman, and R. E. Prange. Chaos, quantum recurrences and Anderson localization. *Physical Review Letters*, 49:509, 1982.

[28] M. C. Gutzwiller. *Chaos In Classical And Quantum Mechanics*. Springer, 1990.

[29] F. Haake. *Quantum Signatures of Chaos, 2nd edition*. Springer, 1991.

[30] S. Habib, K. Shizume, and W. H. Zurek. Decoherence, chaos and the correspondence principle. *Physics Review Letters*, 80:4361, 1998.

[31] J. K. Hale. *Ordinary Differential Equations*. Krieger, 1980.

[32] B. Hu, B. Li, J. Liu, and J. Zhou. Squeezed state dynamics of kicked quantum systems. *Physical Review E*, 58:1743, 1998.

[33] K. Husimi. Some formal properties of the density matrix. *Proceedings of the Physico-Mathematical Society of Japan*, 22:264, 1940.

[34] A. Iomin and G. M. Zaslavsky. Breaking time for the quantum chaotic attractor. *Physical Review E*, 67:027203, 2003.

[35] J. R. Johansson, P. D. Nation, and F. Nori. Qutip 2: A python framework for the dynamics of open quantum systems. *Computer Physics Communications*, 184(4):1234, 2013.

[36] N. L. Johnson, S. Kotz, and N. Balakrishnan. *Continuous Univariate Distributions, Volume 1*. Wiley, 1994.

[37] C. Kittel. *Introduction to Solid State Physics*. Wiley, 1996.

[38] A. R. Kolovsky, H. J. Korsch, and E.-M. Graefe. Bloch oscillations of Bose–Einstein condensates: Quantum counterpart of dynamical instability. *Physical Review A*, 80:023617, 2009.

[39] K. L. Kouptsov, J. H. Lowenstein, and F. Vivaldi. Quadratic rational rotations of the torus and dual lattice maps. *Nonlinearity*, 15:1795, 2002.

[40] L. D. Landau and E. M. Lifshitz. *Mechanics, 3rd. edition*. Pergamon Press, 1976.

[41] D. Leibfried, R. Blatt, C. Monroe, and D. Wineland. Quantum dynamics of single trapped ions. *Reviews Of Modern Physics*, 75:281, 2003.

[42] G. Lindblad. On the generators of quantum dynamical semigroups. *Communications in Mathematical Physics*, 48:119, 1976.

[43] J. H. Lowenstein. Sticky orbits of a kicked harmonic oscillator. *Journal of Physics: Conference Series*, 7:68, 2005.

[44] J. H. Lowenstein. *Pseudochaotic Kicked Oscillators: Renormalization, Symbolic Dynamics, and Transport*. Springer, 2012.

[45] R. M. May. Simple mathematical models with very complicated dynamics. *Nature*, 261:459, 1976.

[46] F. Meinert et al. Interaction-induced quantum phase revivals and evidence for the transition to the quantum chaotic regime in 1D atomic Bloch oscillations. *Physical Review Letters*, 112:193003, 2014.

[47] J. E. Moyal and M. S. Bartlett. Quantum mechanics as a statistical theory. *Mathematical Proceedings of the Cambridge Philosophical Society*, 45:99, 1949.

[48] J. F. Poyatos, J. I. Cirac, and P. Zoller. Quantum reservoir engineering with laser cooled trapped ions. *Physical Review Letters*, 77:4728, 1996.

[49] E. Schrödinger. Der stetige ubergang von der mikro - zur makromechanik. *Die Naturwissenschaften*, 28:664, 1926.

[50] D. W. Scott. *Multivariate Density Estimation: Theory, Practice, and Visualization*. John Wiley and Sons, New York, Chicester, 1992.

[51] J. C. Sprott. *Chaos and Time-Series Analysis*. Oxford University Press, 2003.

[52] J. von Neumann. *Mathematical Foundations of Quantum Mechanics*. Princeton University Press, 1955.

[53] H. Weyl. *The Theory of Groups and Quantum Mechanics*. Dover Publications, New York Inc, 1931.

[54] N. Wheeler. Remarks Concerning the Status and Some Ramifications of Ehrenfest's Theorem. http://academic.reed.edu/physics/faculty/wheeler/documents/Quantum%20Mechanics/Miscellaneous%20Essays/Ehrenfest's%20Theorem.pdf, 1998.

[55] E. P. Wigner. On the quantum correction for thermodynamic equilibrium. *Physical Review*, 40:749, 1932.

[56] Y. Wu and X. Yang. Strong-coupling theory of periodically driven two-level systems. *Physical Review Letters*, 98:013601, 2007.

[57] C. Zachos, D. Fairlie, and T. Curtright. *Quantum Mechanics in Phase Space*. World Scientific, Singapore, 2005.

[58] G. M. Zaslavsky, A. A. Chernikov, R. Z. Sagdeev, and D. A. Usikov. *Weak Chaos and Quasi-regular Patterns*. Cambridge University Press, 1991.

[59] A. I. Zayed. *Handbook of Function and Generalized Function Transformations*. CRC Press, 1996.

A Code for Generating the Figures

This appendix contains the code for generating the various figures in this thesis. We wrote all the code Python and made use of common open-source mathematics libraries, notably NumPy, SciPy, Matplotlib and QuTiP [35], an open-source library that provides methods for examining quantum systems. We present only the code that was used for the sawtooth potential, as the code for the cosine potential is virtually identical.

A.1 Plotting the Classical Kick-to-Kick Mappings

```
from numpy import *
import matplotlib.pyplot as plt

## The kick to kick mapping ##
def mapping((v,u), L, alpha, Gamma):
    return( exp(Gamma)*( v*cos(alpha) + sin(alpha)*(u + L*(floor(v) v)) ), exp
        (Gamma)*( cos(alpha)*(u + L*(floor(v) v)) )   v*sin(alpha) ) )

## Parameters ##
N = 10000 # number of kicks to simulate
q = 6
alpha = 2*pi/q # dimensionless ratio between frequencies
L = 0.1 # nonlinearity parameter
Gamma = 0 # dissipation strength

## Initial condition ##
(v,u)=(1,1)

## Evolve system for N kicks ##
points = [[v,u]]
for n in range(1,N 1):
    (v,u) = mapping((v,u), L, alpha, Gamma)
    points.append([v,u])

xs = [v for [v,u] in points]
ys = [u for [v,u] in points]

## Plotting ##
plt.plot(xs, ys, marker='.', color='r', linestyle='None')
plt.xlim([ 2, 2])
plt.ylim([ 2, 2])
plt.xlabel('v')
plt.ylabel('u')
plt.show()
```

A.2 Plotting the Classical PDFs

```
from numpy import *
import matplotlib.pyplot as plt
from scipy import stats
```

```
def mapping(n, (v0,u0), L, alpha, Gamma):
    (v,u) = (v0,u0)
    for i in range(0, n):
        (v,u) = ( exp(Gamma)*( v*cos(alpha) + sin(alpha)*(u + L*(floor(v) v)) )
            , exp(Gamma)*( cos(alpha)*(u + L*(floor(v) v) )   v*sin(alpha) ) )
    return (v,u)

## Parameters ##
N = 10**5 # number of initial conditions
n = 9 # number of kicks to simulate
L = 6 # nonlinearity parameter
q = 6
alpha = 2*pi/q
Gamma = 0.36 # dissipation strength

## Normally distributed sample of initial conditions ##
xs = random.normal(size=N)
ps = random.normal(size=N)

## Evolve all trajectories ##
for i in range(0,N 1):
    (v0,u0) = (xs[i],ps[i])
    (v,u) = mapping(n, (v0,u0), L, alpha, Gamma)
    xs[i] = v
    ps[i] = u

## Size of phase space to consider ##
xmin =  7#xs.min()
xmax = 2#xs.max()
pmin =  4#ps.min()
pmax = 5#ps.max()

## Draw mesh grid and calculate the PDF using kernel density estimation ##
X, P = mgrid[xmin:xmax:1000j, pmin:pmax:1000j]
positions = vstack([X.ravel(), P.ravel()])
values = vstack([xs, ps])
kernel = stats.gaussian_kde(values)
Z = reshape(kernel(positions).T, X.shape)

## Plot PDF ##
fig, ax = plt.subplots()
cont = ax.imshow(rot90(Z),  extent=[xmin, xmax, pmin, pmax]) #cmap=plt.cm.
    gist_earth_r,
ax.set_xlim([xmin, xmax])
ax.set_ylim([pmin, pmax])
cb = fig.colorbar(cont, spacing='uniform') # add colour bar
plt.xlabel('v')
plt.ylabel('u')
plt.show()
```

A.3 Calculating and Plotting the Maximum LE

```
from numpy import *
import matplotlib.pyplot as plt
```

```
# The mappings v and u
def mapping((v,u), K, alpha, Gamma):
    return ( exp( Gamma)*(v*cos(alpha) + sin(alpha)*(u + K*(floor(v) v))), exp
        ( Gamma)*(cos(alpha)*(u + K*(floor(v) v))   v*sin(alpha)) )

# Euclidian Distance
def dist((x1,y1),(x2,y2)):
    return sqrt( (x1 x2)**2 + (y1 y2)**2 )

# Calculate the highest Lyapunov Exponent for a single initial condition
def exponent(K, q, Gamma, d0, (v0,u0)):
    # Step 1: Evolve initial condition for 100 steps to ensure it is on the
        attractor
    for n in range (0, 99):
        (x, y) = mapping((v0,u0), K, q, Gamma)


    # Step 2: Choose a point (v,u) at distance d0 from (vn, un)
    (v, u) = ( x + d0*np.cos(np.pi/4), y + d0*np.sin(np.pi/4) )

    # We repeat the next steps over 100000 iterations
    exps = [] # the exponents we calculate and wish to average
    for i in range(0, 100000):
        # Step 3: Advance both orbits one iteration and calculate the new
            separation d1
        (x, y) = mapping(1, (x,y), K, q, Gamma)
        (v, u) = mapping(1, (v,u), K, q, Gamma)
        d1 = dist((x,y),(v,u))

        # Step 4: Calculate log|d1/d0|
        d = abs(d1/d0)
        exps.append(log(d))

        # Step 5: Readjust one orbit so its separation is d0 and it is in the
            same direction as d1
        (v, u) = ( x + d0*(v x)/d1, y + d0*(u y)/d1 )

    return sum(exps)/len(exps) # return average value of the LE

# Generate a uniformly distributed set of N points (x, y) with low <= x,y <
    high
def generate(N, low, high):
    output = []
    for i in range(0, N):
        output.append( (random.uniform(low, high), random.uniform(low, high)) )
    return output

# Calculate the highest Lyapunov Exponent averaged over N initial conditions
def averagedExponent(K, q, Gamma, d0, N):
    inits = generate(N, 0, 100)
    exps = [] # the exponents we calculate and wish to average
    for point in inits:
        exps.append( exponent(K, q, Gamma, d0, point) )
```

```
    return sum(exps)/len(exps) # return average value of the LE

# Parameters
q = 6
alpha = 2*pi/q
N = 10000
d0 = 0.00000000001
L = arange(0., 10., 0.1)
Gamma = 0

# Plotting
plt.plot(Gamma, averagedExponent(L, q, Gamma, d0, N), color='k')
plt.axhline(linewidth=1, color='r') # plot a red line through the origin to
    guide the eye
plt.xlabel(r'$\Gamma\ \tau/2$')
plt.ylabel(r'$\lambda$')
plt.show()
```

A.4 Drawing the Bifurcation Diagrams

```
from numpy import *
import matplotlib.pyplot as plt

# The mappings v and u
def mapping(n, (v0,u0), L, alpha, Gamma):
    (v,u) = (v0,u0)
    for i in range(0, n):
        (v,u) = ( exp( Gamma)*(v*cos(alpha) + sin(alpha)*(u + L*(floor(v) v))),
            exp( Gamma)*(cos(alpha)*(u + L*(floor(v) v))   v*sin(alpha)) )
    return (v,u)

# Parameters
L = 6
q = 6
alpha = 2*pi/q

# Label axes
plt.xlabel(r'$\Gamma\ \tau/2$')
plt.ylabel('u')

# Override plots autoscaling
plt.ylim(( 2,2))

# Set the initial condition used across the different parameters
ic = (1,1)

# Set up transients and iterates
nTransients = 10000
nIterates = 1000
nSteps = 200

# Sweep the control parameter over the desired range
inc = 1/float(nSteps)
for Gamma in arange(0,2,inc):
```

```
        # Set the initial condition to the reference value
        state = ic
        # Throw away the transient iterations
        state = mapping(nTransients, state, L, alpha, Gamma)
        # Now store the next batch of iterates
        Gammasweep = [ ]   # The parameter value
        u = [ ]         # The iterates
        for i in xrange(nIterates):
                state = mapping(1, state, L, alpha, Gamma)
                Gammasweep.append(K)
                u.append( state[1] )
        plt.plot(Gammasweep, u, 'k,') # Plot the list of (Gamma,u) pairs as
            pixels

# Display plot in window
plt.show()
```

A.5 Plotting the Conservative Wigner Function

```
from qutip import *
from numpy import *
import matplotlib.pyplot as plt

## Return the cosine of an operator ##
def cosine(Op):
    return 0.5*( (i*Op).expm() + ( i*Op).expm() )

## The sawtooth potential with j=1 to M ##
def sawtooth(x, M):
    output = 0
    for j in range (1, M):
        output = output + (1/(j**2))*cosine(j*x)
    return output

## Parameters ##
i = 1.0j # imaginary unit
n = 9 # number of kicks to simulate
L = 6 # classical dimensionless kick strength
q = 6
alpha = 2*pi/q # dimensionless ratio between frequencies
sigma = 0.1 # classicality parameter
M = 1000 # number of terms in the sum
N = 2**8 # number of states of quantum system

Lq = (pi*L)/(sigma**2) # quantum kick strength

## Basis State ##
rho = coherent_dm(N, 0)

## Operators ##
a = destroy(N) # lowering operator

F0 = ( i*alpha*(a.dag()*a + 0.5)).expm()
```

```
F1 = ( i*Lq*sigma*(a + a.dag())/2   i*Lq*sawtooth(sigma*(a + a.dag()), M)/pi).
    expm()
F = F0*F1 # Floquet operator

## Apply Floquet operator n times to get state before (n+1)th kick ##
for u in range(1, n):
    rho = F * rho * F.dag()

## Plot Wigner Function ##
xvec = linspace(20,20,500) # range of phase space
W = wigner(rho, xvec, xvec) # generate Wigner Function

fig, axes = plt.subplots()  # set up axis and figure
cont = axes.contourf(xvec, xvec, W, 1000) # plot Wigner Function
plt.xlabel('v')
plt.ylabel('u')
cb = fig.colorbar(cont, ax=axes) # add colour bar
plt.show()
```

A.6 Plotting the Dissipative Wigner Function

```
from qutip import *
from numpy import *
import matplotlib.pyplot as plt
from scipy import ndimage

## Return the cosine of an operator ##
def cosine(Op):
    return 0.5*( (i*Op).expm() + ( i*Op).expm() )

## The sawtooth potential with j=1 to M ##
def sawtooth(x, M):
    output = 0
    for j in range (1, M):
        output = output + (1/(j**2))*cosine(j*x)
    return output

## Parameters ##
i = 1.0j # imaginary unit
n = 10 # number of kicks to simulate
L = 6 # classical dimensionless kick strength
q = 6
alpha = 2*pi/q # dimensionless ratio between frequencies
sigma = 0.1 # classicality parameter
M = 1000 # number of terms in the sum
N = 2**8 # number of states of quantum system
Lq = (pi*L)/(sigma**2) # quantum kick strength
Gamma = 0.36

## Coherent State centred at the origin ##
rho = coherent_dm(N,0)

## Operators ##
a = destroy(N) # lowering operator
```

```
v = 0.5*(a + a.dag())
u = 0.5*i*(a.dag()    a)
H = a.dag()*a
F1 = ( i*Lq*sigma*(a + a.dag())/2).expm()
F2 = ( i*Lq*sawtooth(sigma*(a + a.dag()), M)/pi).expm()
F = F1*F2 # Floquet operator

S = ( i*alpha*(spre(H) spost(H)) + 2*Gamma*lindblad_dissipator(a)).expm() #
    superoperator

## Apply Evolution n times to get state before (n+1)th kick ##
for j in range(0, n 1):
   rho = vector_to_operator(S * operator_to_vector(F * rho * F.dag()))

print variance(v, rho)
print variance(u, rho)

## Plot Wigner Function ##
xvec = linspace( 10,10,500)
W = wigner(rho, xvec, xvec) # generate Wigner Function
fig, axes = plt.subplots()  # set up axis and figure
cont = axes.contourf(xvec, xvec, W, 1000) # plot Wigner Function
plt.xlim([ 7,2])
plt.ylim([ 3,4])
plt.xlabel('v')
plt.ylabel('u')
cb = fig.colorbar(cont, spacing='uniform',ax=axes) # add colour bar
plt.show()
```

A.7 Numerical Calculation of Breaking Time

```
from numpy import *
import matplotlib.pyplot as plt
from qutip import *

## Classial kick to kick mapping ##
def mapping((v,u), L, alpha, sigma, Gamma):
   w = v*(sigma/pi)
   return ( exp( Gamma)*( v*cos(alpha) + sin(alpha)*(u + (L*pi/sigma)*(floor(w
       ) w)) ), exp( Gamma)*( cos(alpha)*(u + (L*pi/sigma)*(floor(w) w) )   v*
       sin(alpha) ) )

def sawtooth(x, M):
   output = 0
   for j in range (1, M):
      output = output + (1/(j**2))*cosine(j*x)
   return output

## Cosine of an operator ##
def cosine(Op):
   return 0.5*( (i*Op).expm() + ( i*Op).expm() )

## The breaking time we obtained from analysis ##
def analyticw(L, sigma):
```

```
    return 2/(3*L*sigma)

## The metric d_r ##
def dist(psi, xs):
    a = destroy(N)
    v = 0.5*(a + a.dag()) # position operator
    deltaq = variance(v, psi)
    deltacl = xs.var()
    return abs((deltacl deltaq)/deltacl)

## Method for calculating the breaking time for a single eta ##
def breakingTime(n, L, alpha, sigma, N):
    i = 1.0j # imaginary unit
    traj = 10**4 # number of classical trajectories
    epsilon = 0.1 # threshold for divergence of the distributions
    Lq = (pi*L)/(sigma**2) # quantum kick strength
    M = 100

    ## Operators ##
    a = destroy(N) # lowering operator
    F0 = ( i*alpha*(a.dag()*a + 0.5)).expm()
    F1 = ( i*Lq*sigma*(a + a.dag())).expm()
    F2 = ( i*Lq*sawtooth(sigma*(a + a.dag()), M)/pi).expm()
    F = F0*F1*F2 # Floquet operator

    ## Normally distributed sample of initial conditions ##
    xs = random.normal(loc=0, scale=0.5, size=traj)
    ps = random.normal(loc=0, scale=0.5, size=traj)

    ## Coherent State centred at (x,p) ##
    psi = coherent(N, 0)

    points = [dist(psi,xs)]

    for l in range (1,n):
        ## Evolve classical state ##
        for k in range(0,traj 1):
            (v0,u0) = (xs[k],ps[k])
            (v,u) = mapping((v0,u0), Lq, alpha, sigma, 0)
            xs[k] = v
            ps[k] = u
        ## Evolve quantum state ###
        psi = F * psi
        d = dist(psi, xs)
        points.append(d)

    ## Find the number of the kick at which d_r first exceeds the threshold
        epsilon ##
    k = 1
    while(points[k] < epsilon and k < n 1):
        k = k+1

    if k < n 1:
        return k
```

```
    else:
        return n


## Parameters ##
i = 1.0j # imaginary unit
n = 100 # number of kicks to simulate
L = 0.1 # classical dimensionless kick strength
alpha = 2*pi/6
N = 2**8 # number of states of quantum system

## Plot the values ##
ss = arange(0.05, 1.0, 0.05)
points = []
for sigma in ss:
    points.append(breakingTime(n, L, alpha, sigma, N))

plt.plot(ss, points, color='k', linestyle='None', marker='.')
plt.plot(ss, analyticw(L, ss), color='b')
plt.ylim([0,100])
plt.xlabel(r'$\sigma$')
plt.ylabel(r'$t_\hbar$')
plt.show()
```